MAY 0 6 1987

AEDC-TR-67-226

# IN SITU MEASUREMENT OF THICKNESS AND OTHER PROPERTIES OF CARBON DIOXIDE CRYODEPOSITS BY OPTICAL TECHNIQUES

K. E. Tempelmeyer, B. E. Wood, and D. W. Mills, Jr.

ARO, Inc.

December 1967

This document has been approved for public release and sale; its distribution is unlimited.

AEROSPACE ENVIRONMENTAL FACILITY
ARNOLD ENGINEERING DEVELOPMENT CENTER
AIR FORCE SYSTEMS COMMAND
ARNOLD AIR FORCE STATION, TENNESSEE

# NOTICES

When U. S. Government drawings specifications, or other data are used for any purpose other than a definitely related Government procurement operation, the Government thereby incurs no responsibility nor any obligation whatsoever. and the fact that the Government may have formulated, furnished, or in any way supplied the said drawings, specifications, or other data, is not to be regarded by implication or otherwise, or in any manner licensing the holder or any other person or corporation, or conveying any rights or permission to manufacture, use, or sell any patented invention that may in any way be related thereto.

Qualified users may obtain copies of this report from the Defense Documentation Center.

References to named commercial products in this report are not to be considered in any sense as an endorsement of the product by the United States Air Force or the Government.

# IN SITU MEASUREMENT OF THICKNESS AND OTHER PROPERTIES OF CARBON DIOXIDE CRYODEPOSITS BY OPTICAL TECHNIQUES

K. E. Tempelmeyer, B. E. Wood, and D. W. Mills, Jr.
ARO, Inc.

This document has been approved for public release and sale; its distribution is unlimited.

AF - AEDC
Arnold AFB Tenn

## FOREWORD

The research reported herein was sponsored by Arnold Engineering Development Center (AEDC), Air Force Systems Command (AFSC), Arnold Air Force Station, Tennessee, under Program Element 6144501F, Project 8951, Task 895104.

The results of the research were obtained by ARO, Inc. (a subsidiary of Sverdrup & Parcel and Associates, Inc.), contract operator of AEDC, AFSC, under Contract AF40(600)-1200. The work was performed under ARO Project No. SW5703 from January 1 to July 31, 1967, and the manuscript was submitted for publication on September 28, 1967.

The authors would like to thank Dr. Frank Collins, Brooklyn Polytechnic Institute and Dr. Allie Smith, ARO, Inc., for many valuable suggestions during the course of this investigation.

This technical report has been reviewed and is approved.

Fred W. Alles
1/Lt, USAF
Research Division
Directorate of Plans
and Technology

Edward R. Feicht
Colonel, USAF
Director of Plans
and Technology

## ABSTRACT

Measurements of interference patterns in filtered light reflected from thin 77°K $CO_2$ cryodeposits are reported. Analysis indicated that these patterns are a result of interference between light rays scattered by reflection from the cryodeposit surface with rays which are scattered by passage through the surface and specularly reflected by the substrate. A simple light scattering model for cryodeposits is proposed which allows accurate determination of the deposit thickness from the interference patterns. Application of the scattering theory required knowledge of the refractive index of the cryodeposit. Consequently, the index of refraction for $CO_2$ cryodeposits was determined from separate Bragg interference tests at wavelengths from 0.6 to 1.0 $\mu$. Cryodeposit thicknesses up to 100 $\mu$ have been determined from the scattering model equation. Utilizing mass conservation principles, the thickness calculations were further used to determine the mean cryodeposit density. A few scattering interference tests on other types of cryodeposits are also briefly reported.

## CONTENTS


| | | Page |
|---|---|---|
| | ABSTRACT | iii |
| | NOMENCLATURE | vii |
| I. | INTRODUCTION | 1 |
| II. | LIGHT SCATTERING THEORY FOR CRYODEPOSITS | 2 |
| III. | EXPERIMENTAL APPARATUS | |
| | 3.1 Vacuum Chamber | 6 |
| | 3.2 Gas Addition System | 6 |
| | 3.3 Light Source and Detectors | 7 |
| | 3.4 Instrumentation | 7 |
| IV. | EXPERIMENTAL PROCEDURE AND RESULTS | |
| | 4.1 Scattering Experiments | 7 |
| | 4.2 Bragg-Refraction Experiments | 9 |
| | 4.3 Additional Tests | 11 |
| V. | DISCUSSION | |
| | 5.1 Refractive Index Measurement | 12 |
| | 5.2 Verification of Scattering Theory | 12 |
| | 5.3 Thickness Measurements | 15 |
| | 5.4 Density Measurements | |
| | 5.5 Measurements on Other Types of Films | 16 |
| | 5.6 Measurements with Laser Light Source | 16 |
| VI. | CONCLUSIONS | 17 |
| | REFERENCES | 19 |


## APPENDIXES

I. ILLUSTRATIONS


| Figure | | |
|---|---|---|
| 1. | Typical Interference Scattering Pattern for Thin $CO_2$ Cryodeposits | 23 |
| 2. | Schematic of Light Scattering Model | 24 |
| 3. | Schematic of Experimental Apparatus | 25 |
| 4. | Photograph of 200-$cm^2$ Polished Copper Cryosurface | 26 |
| 5. | Photograph of Heating Jacket | 27 |

| Figure | | Page |
|---|---|---|
| 6. | Filter Transmission Characteristics | 28 |
| 7. | Detector Output-Wavelength Spectrum of Light Source, Filter, Solar Cell Detector System | 29 |
| 8. | Scattering Interference Patterns for Normal Incidence and a $CO_2$ Input-Rate of 1.25 $cm^3/sec$ | 30 |
| 9. | Scattering Interference Patterns for Normal Incidence and a $CO_2$ Input Rate of 0.126 $cm^3/sec$ | 31 |
| 10. | Scattering Interference Patterns for Normal Incidence and a $CO_2$ Input Rate of 0.0145 $cm^3/sec$ | 32 |
| 11. | Effect of Wavelength on Scattering Interference Patterns for $CO_2$ Cryodeposits at $P = 2.1 \times 10^{-2}$ torr. | 33 |
| 12. | Effect of Wavelength on Scattering Interference Patterns for $CO_2$ Cryodeposits at $P = 4.1 \times 10^{-4}$ torr. | 35 |
| 13. | Scattering Interference Patterns for $CO_2$ Cryodeposits with Nonnormal Incident Radiation. | 36 |
| 14. | Bragg Refraction Patterns for $CO_2$ Cryodeposits with Various Wavelengths of Incident Radiation | 37 |
| 15. | Bragg Refraction Patterns for $CO_2$ Cryodeposits Formed at Various Pressure Levels | 38 |
| 16. | Measured Refractive Index for $CO_2$ Cryodeposits at Various Pressure Levels and Wavelengths | 39 |
| 17. | Variation of Refractive Index of $CO_2$ Cryodeposit with Wavelength | 40 |
| 18. | Bragg Interference from 77°K $CO_2$ Cryodeposits on a Black Substrate | 41 |
| 19. | Angular Distribution of Light from a 77°K $CO_2$ Cryodeposit on a Black Substrate | 42 |
| 20. | Comparison of Calculated Thicknesses | 43 |
| 21. | Calculation of nth Order Peak Locations | 44 |
| 22. | Comparison of Various Methods of Computing Cryodeposit Thicknesses | 45 |
| 23. | Comparison of Cryodeposit Thickness Determined with Incident Radiation at Two Angles | 46 |

Figure | Page

24. Effect of Gas Addition Rate on Cryodeposit Thickness . . . . . 47

25. Effect of Gas Addition Rate on Cryodeposit Thickness . . . . . 48

26. Density of $CO_2$ Cryodeposits at Various Pressures . . . . . 49

27. Scattering Interference Patterns for 77°K $H_2O$ Cryodeposits at Two Thicknesses . . . . . 50

28. Bragg and Scattering Interference Patterns for 77°K Cryodeposits of Diffusion Pump Oil . . . . 51

29. Scattering Interference Patterns of $CO_2$ Cryodeposit with a Laser Light Source . . . . . 52

II. METHODS OF CALCULATION . . . . . 53

## NOMENCLATURE

| | |
|---|---|
| $A_s$ | Area of cryosurface |
| K | Thickness growth constant |
| $\ell_{AB}$ | Path length from point A to point B |
| $\dot{m}$ | Mass flow rate |
| n, m, q | Integers |
| p | Pressure |
| R | Gas law constant |
| T | Temperature |
| t | Time |
| $t_s$ | Specular component of ray transmitted through the surface into the film |
| $\dot{V}$ | Volumetric flow rate |
| $V_a$ | Volume of gas added to chamber |
| $\beta_i$ | Angle of incidence |
| $\beta_n$ | Angle at which reflected energy is measured (see Fig. 2) |

| | |
|---|---|
| $\beta_r$ | Specular angle of reflection |
| $\theta_i$ | Angle of refraction within the film (see Fig. 2) |
| $\theta_n$ | Angle of scattered ray within cryodeposit |
| $\lambda$ | Wavelength |
| $\mu$ | Refractive index |
| $\mu_v$ | Refractive index in a vacuum = 1.0 |
| $\tau$ | Film thickness |

**SUBSCRIPTS**

| | |
|---|---|
| a | Added |
| c | Cryodeposit |
| f | Forward of leak |
| m | Value at maximum |

# SECTION I
# INTRODUCTION

Most large thermal-vacuum space simulation chambers employ cryogenic pumping and, consequently, the test vehicle is surrounded by panels cooled to near 77°K by liquid nitrogen. These panels are normally painted black to minimize the reflection of radiation from the solar simulator. However, as carbon dioxide and water vapor frost films form on the panels because of cryopumping, the reflective characteristics of the panels change and the test vehicle thermal balance is altered. For these reasons, the reflective characteristics of cryodeposits are being systematically investigated at the Arnold Engineering Development Center (AEDC) (Refs. 1 through 3).

One phase of this program is the measurement of the angular distribution of light reflected from cryodeposits formed on a 77°K surface. These measurements have shown that the specular component of light reflected from a cryosurface steadily decreases as the cryodeposit thickness increases (Ref. 3). Ultimately, light is reflected from cryodeposits in a diffuse manner. While making measurements of the angular distribution of reflected light, various interference-type patterns were also observed. An example of one of these patterns is sketched in Fig. 1. Since the intensity of the observed interference peaks was two or three orders of magnitude lower than the maximum intensity of the specularly reflected light, these interference phenomena are unimportant in so far as the test vehicle thermal balance is concerned. However, they have been investigated further to obtain a better understanding of the light scattering properties of cryodeposits and because they may have application to in situ measurement of cryodeposit thickness and contamination films in space chambers.

Cryodeposit light scattering phenomena are analyzed in this report, and a simple scattering model is proposed. Test results obtained for $CO_2$ cryodeposits formed at various rates and at pressure levels from $7 \times 10^{-5}$ to 10 torr are also presented. Analysis of these data with the proposed models leads to determination of the thickness, index of refraction, and density of $CO_2$ cryodeposits. A few test results obtained with water vapor and diffusion pump oil cryodeposits are also given to demonstrate other applications of the proposed in situ optical measuring technique.

## SECTION II
## LIGHT SCATTERING THEORY FOR CRYODEPOSITS

Previous measurements (Ref. 3) have shown that a specularly reflecting surface will reflect light diffusely when coated with a $CO_2$ cryodeposit. These tests suggest that the cryodeposit surface may be optically rough and that light may be internally scattered within the cryodeposit itself. In addition, the observed interference patterns (Fig. 1 - Appendix I) were always accompanied by strong specular peaks. This indicates that interference occurred when the deposits were optically thin and the effect of the substrate was still pronounced. For this reason, internal scattering and absorption have been neglected in the light scattering model proposed here, and the basic assumption is that light is scattered by reflection from and passage through the cryodeposit surface. In addition, the following assumptions have been made:

1. The incident light beam is perfectly collimated and monochromatic.
2. The substrate is a perfect specular reflector.
3. Cryodeposits refract light according to Snell's Law.
4. An abrupt 180-deg phase shift occurs when light passing through one media is reflected by another which has a higher refractive index (see Ref. 4).
5. There is no gap, cavity, or contamination between the cryodeposit and substrate.

A sketch of the scattering model is shown in Fig. 2. The incident beam strikes the surface at point A at an angle $\beta_i$ from the substrate normal. It is assumed that a portion of the beam is directly reflected from the surface and is scattered into a family of rays which, for convenience, will be called the r-family. The distribution of the r-family is unknown; however, it probably resembles the distribtion shown in Fig. 2. The wave fronts corresponding to the reflected rays undergo a 180-deg phase shift, since the refractive index of the cryodeposit is greater than unity.

Light which is transmitted through the surface is refracted according to Snell's Law and assumed to scatter into say the t-family of rays. Again, the distribution of the t-family is not known, but it is made up of a refracted component, ray $t_s$, and an infinite number of other scattered t-rays. Any arbitrary scattered t-ray, $t_1$, is assumed to be specularly reflected by the substrate at point B with a 180-deg phase shift. Part of

this reflected ray (BC) is retransmitted and refracted by the surface at C and scattered into another family of rays (the s-family). Again, the s-family has a refracted component (ray CL) and an infinite number of other scattered rays, as shown in Fig. 2. Although not shown in the figure, the other part of ray BC is reflected and scattered at C. There are subsequent reflections, transmissions, and scattering of this latter part, but these will only reproduce at lower intensity the effects described below.

In this simple "first-order" theory we will only consider the refracted component of the s-family (i.e., ray CL). Other s-family rays correspond to the scattering of a scattered ray.* Their effects are assumed to be second order and are neglected. The arbitrarily chosen $t_1$ ray lies at an angle $\theta_n$ with respect to the substrate normal, and its refracted component, ray CL, lies at the angle $\beta_n$ from the normal. Angles $\beta_n$ and $\theta_n$ are related by Snell's Law. Because waves in both the r-family and the s-family have both undergone 180-deg phase shifts, ray CL will constructively interfere with that ray in the r-family which is at an angle $\beta_n$ from the normal (i.e., ray AD) if:

$$\mu \ell_{ABC} - \ell_{AD} = m\lambda \tag{1}$$

that is, if their optical path lengths differ by an integer number (m) of wavelengths.

These geometric lengths are easily related to the cryodeposit thickness $\tau$. By inspection of Fig. 2,

$$\cos\theta_n = \frac{2\tau}{\ell_{ABC}} \tag{2}$$

and

$$\sin\beta_n = \frac{\ell_{AD}}{\ell_{AC}} = \frac{\ell_{AD}}{2\tau\tan\theta_n} \tag{3}$$

Since we are only dealing with the refracted component of the s-family,

$$\mu \sin\theta_n = \mu_v \sin\beta_n \tag{4}$$

If the refractive index for the surrounding vacuum, $\mu_V$, is unity, Eqs. (1) through (4) may be combined to give

$$\tau = \frac{m\lambda}{2\mu\sqrt{1 - \frac{\sin^2\beta_n}{\mu^2}}} \tag{5}$$

---

*The one exception to this will be considered later.

Equation (5) expresses the criterion for constructive interference between the specularly reflected, retransmitted, and refracted component of an arbitrary scattered transmitted ray in the t-family and a reflected and scattered ray in the r-family which has the same angle to the normal. The two rays would destructively interfere for half-integer values of m.

There is an infinite number of other scattered rays in the t-family which are specularly reflected from the substrate and then scattered by the cryodeposit surface to produce s-families. For a given cryodeposit thickness, the refracted components of some of these s-families would interfere with particular r-family rays to produce an interference pattern like that shown in Fig. 1. Peaks occur because of constructive interference at discrete angles $\beta_1$, $\beta_2$, $\beta_3$, . . . when Eq. (5) can be simultaneously satisfied by,

$$\begin{aligned} m &= m_1 \text{ for } \beta_1 \\ m &= m_1 - 1 \text{ for } \beta_2 \\ m &= m_1 - 2 \text{ for } \beta_3 \\ &\text{etc.} \end{aligned} \tag{6}$$

Valleys are produced by destructive interference at the intermediate angles corresponding to half integer m's. $m_1$ is not known in advance but for a set of interference peaks (i.e., a set of $\beta_n$'s) a unique value of $m_1$ can be easily found by the method outlined in the Appendix II.

Scattered rays of a given s-family also leave the surface at various values of $\beta_n$ and interfere with the refracted components of other s-families which have the same angle. We have already assumed that they may be neglected as a second-order effect. However, the effect of one special s-family should be examined. It is believed that the t-family distribution must have an intense refracted component, denoted as $t_s$ in Fig. 2. This ray could produce an s-family of scattered rays at point I whose intensities could be comparable to the refracted components of other s-families. Thus, we should consider possible interference between the refracted component of the s-family caused by an arbitrary t-family ray (say ray CL) and a scattered ray in the s-family caused by $t_s$, which has the same angle to the normal (i.e., ray IJ). Referring again to Fig. 2, constructive interference between two such rays with the same angle $\beta_n$ occurs if

$$(\mu \ell_{AHI} + \ell_{IJ}) - \mu \ell_{ABC} = n\lambda \tag{7}$$

The two optical paths in question have about the same length. The first interference peak would occur at $\beta_1$ when these two lengths differ by one wavelength (n = 1); the second peak would occur when the two optical

distances differ by two wavelengths (n = 2), etc. Thus, in this case the integers are known in advance. Equations (2), (3), (4), and (7) together with other similar geometric relationships which may be obtained from Fig. 2 combine to give

$$r = \frac{n\lambda}{2\mu\left[\frac{1}{\sqrt{1-\frac{\sin^2\beta_i}{\mu^2}}} - \frac{\sin\beta_i \sin\beta_n}{\mu^2\sqrt{1-\frac{\sin^2\beta_i}{\mu^2}}} - \sqrt{1-\frac{\sin^2\beta_n}{\mu^2}}\right]} \tag{8}$$

where

$$n = 1, 2, 3, \ldots$$
$$\text{for } \beta_1, \beta_2, \beta_3, \ldots$$

Equation (8) was derived assuming that the light entering the cryodeposit is refracted by Snell's Law.

For convenience, most of the test results were obtained when the light source was normal to the surface, $\beta_i = 0$ deg. In this case, Eq. (5) is unchanged or

$$r = \frac{m\lambda}{2\mu\sqrt{1-\frac{\sin^2\beta_n}{\mu^2}}} \tag{9}$$

$\mu$ = ref. index

$r$ = cryodeposit thickness

and Eq. (8) becomes

$$r = \frac{n\lambda}{2\mu\left[1-\sqrt{1-\frac{\sin^2\beta_n}{\mu^2}}\right]} \tag{10}$$

Equations (5) and (8) then represent (when m and n are whole integers) the conditions for constructive interference between (1) rays along CL and AD and (2) rays along CL and IJ, respectively. It is not possible at this point to determine if either of these two types of interference predominates, since this would require a knowledge of the distribution patterns of all the scattered rays. However, the derived equations may be used to predict the angular position of the interference peaks and valleys, and their application to the measured scattering patterns should illustrate what type of interference is the most significant. Furthermore, this light scattering theory* can be used to determine the

*Equations (5) and (8) or their special cases for normal incidence, Eqs. (9) and (10)

thickness of thin cryodeposits, and once the thickness is known it may be possible to determine cryodeposit densities.

## SECTION III
## EXPERIMENTAL APPARATUS

### 3.1 VACUUM CHAMBER

All tests were conducted in a 30-in.-diam spherical vacuum chamber, schematically shown in Fig. 3. It was assembled from two flanged 30-in. stainless steel hemispheres joined with an O-ring seal. The pumping system (not shown in the figure) consisted fo a 400-$\ell$/min mechanical pump and a 6-in. oil diffusion pump which was equipped with a water-cooled baffle and an $LN_2$-cooled cold cap. A vacuum-rated valve was used to isolate the chamber from the pumping system. The system could be pumped to $1 \times 10^{-6}$ torr.

A 7.6- by 10.2-cm polished copper cryosurface (see Fig. 4) with an rms surface roughness of less than 0.01$\mu$ was located near the center of the chamber. The rear and side surfaces were coated with flat black paint. A rotary vacuum seal was used to rotate the surface to any desired polar angle with respect to the incident light beam. All of the cryodeposits studies were formed on this surface which was cooled with 77°K $LN_2$. For most tests the cryodeposit was allowed to form over the entire cryosurface area, 200 $cm^2$. In some instances a heated jacket was placed around the cryosurface (Fig. 5) such that the cryodeposit could only form on a 63-$cm^2$ area.

The chamber was equipped with a detector arm having a 25-cm radius on which a silicon solar cell was mounted. The arm could be remotely rotated at constant angular velocity about the surface, thereby mapping the distribution of the reflected radiation. The interior surface of the chamber was also coated with flat black paint to minimize the effect of any reflections not coming from the polished test surface.

### 3.2 GAS ADDITION SYSTEM

Carbon dioxide with a purity level of 99.8 percent was introduced into the vacuum sphere by means of a calibrated leak system. The gas was supplied to a reservoir which maintained an essentially constant forepressure of 760 torr to the leaks. The three available leaks were calibrated at the operating forepressure and at backpressures spanning

the range covered in the experiment. They had volumetric flow rates of 1.25, 0.126, and 0.0145 $cm^3/sec$.

### 3.3 LIGHT SOURCE AND DETECTORS

Electromagnetic radiation was provided by a xenon lamp and focused by means of a condensing lens system. It was introduced into the chamber through a quartz window and a collimating tube, as shown in Fig. 3. Interference-type filters could be inserted between the condensing lens system and the quartz window to obtain a quasi-monochromatic beam. The transmission characteristics of some of these filters are shown in Fig. 6. A silicon solar cell detector was used.

The composite spectral distribution of the xenon lamp, beam collimating lens, filter, and detection system is given in Fig. 7. Data in Fig. 7 were obtained by removing the cryosurface from the chamber, aligning the detector to intercept the light beam, and measuring the maximum detector output as different filters were inserted.

### 3.4 INSTRUMENTATION

The chamber pressure was measured with a conventional ionization gage or an Alphatron® depending upon the test pressure level, and the forepressure on the leak was read on a Wallace-Tiernan gage.

## SECTION IV
## EXPERIMENTAL PROCEDURE AND RESULTS

Two types of measurements were made on the $CO_2$ cryodeposits. For convenience, these will be referred to as a scattering experiment and a Bragg refraction experiment. Each produced a different type of interference pattern.

### 4.1 SCATTERING EXPERIMENTS

The chamber was pumped to about $1 \times 10^{-6}$ torr and valved off from the pumping system. Then, the xenon lamp was turned on, and the test surface rotated to the desired angle with respect to the incident light beam. For most of the scattering tests, the incident light was normal to the test surface. Alignment was achieved by rotating the surface until the reflection patterns were symmetrical.

For nonnormal incident radiation, the incidence angle was approximately set with a protractor indexing device and then measured to within ±0.2 deg from the reflection versus angle record. The test surface was then cooled to about 77°K. When the surface temperature reached equilibrium, the detector arm was rotated through an arc of about 60 to -60 deg with respect to the surface normal and a reference trace of the angular distribution of reflected light made at various wavelengths.

Cryodeposit films were formed by flowing $CO_2$ into the chamber, through the desired leak, for a specified time. After the $CO_2$ was cryopumped on the test surface, the angular distribution of reflected light was again recorded at the nominal wavelengths provided by the filters (see Fig. 6). Two types of films were produced:

1. Multilayered films formed by putting a cryodeposit layer on top of previous layers, or
2. Monolayered* films formed as a single continuous deposit.

At pressures above about $5 \times 10^{-4}$ torr, the cryodeposits were formed with a helium gas background. The chamber was pumped to the lowest possible pressure (about $10^{-6}$ torr), valved off, and refilled with laboratory grade helium to the desired pressure level.

Some typical interference patterns measured with this procedure are presented in Figs. 8 through 13. The variables covered in these particular experiments are summarized in the following table:

| Figure | Wavelength $\lambda, \mu$ | $CO_2$ Addition Rate, $cm^3/sec$ | Flow Time, min | Pressure Level, torr | Cryosurface Area, $cm^2$ | $\beta_i$ deg | Remarks |
|---|---|---|---|---|---|---|---|
| 8 | 0.7, 0.8 0.9 & 1.0 | 1.25 | 0 to 6 | $1.6 \times 10^{-4}$ | 200 | 0 | Multi-layers |
| 9 | " | 0.126 | 0 to 36 | $1.3 \times 10^{-4}$ | 200 | 0 | " |
| 10 | " | 0.0145 | 0 to 360 | $1.0 \times 10^{-4}$ | 200 | 0 | " |
| 11a | 0.8, 0.9 & 1.0 | 0.126 | 4.67 | $2.1 \times 10^{-2}$ | 63 | 0 | Mono-layer |
| 11b | " | 0.126 | 9.50 | $2.1 \times 10^{-2}$ | 63 | 0 | " |
| 12 | 0.7, 0.9 0.9 & 1.0 | 0.126 | 6.23 | $4.1 \times 10^{-4}$ | 63 | 0 | " |
| 13 | 0.8 0.9 & 1.0 | 0.126 | 6.23 | $4.0 \times 10^{-4}$ | 63 | 21.5 | " |

*A monolayer is defined here as a cryodeposit formed in a continuous manner rather than the common definition of a single layer of molecules.

It should be noted that specular peaks existed about $\beta_n = 0$ deg for the distribution patterns presented in Figs. 8 through 12 and about $\beta_n = -21.5$ deg for the distributions given in Fig. 13. They were about two to three orders of magnitude more intense than the levels shown. The "valleys" at $\beta_n = 0$ deg in Figs. 11 and 12 and at $\beta_n = 21.5$ deg in Fig. 13 were caused by the rotating detector arm intercepting and cutting off the incident light beam.

## 4.2 BRAGG-REFRACTION EXPERIMENTS

Equations (5) and (8) or their special cases for normal incidence, Eqs. (9) and (10), involve two unknowns, the cryodeposit thickness, $\tau$, and refractive index, $\mu$. Consequently, a series of Bragg refraction measurements was made to determine the refractive index.

Figure 2 shows that the refracted component of the s-family produced by the specular reflection of ray $t_s$ would lie along IF at an angle $\beta_r = -\beta_i$ from the normal. It would interfere with that ray in the reflected r-family which leaves the surface at $\beta_r$ (i.e., ray AK) if,

$$\mu \ell_{AHI} - \ell_{AK} = q\lambda$$

where q is an integer. This is a statement of the Bragg Reflection-Refraction Law and in terms of measurable quantities may be expressed,

$$\tau = \frac{q\lambda}{2\mu\sqrt{1 - \frac{\sin^2\beta_i}{\mu^2}}} \tag{11}$$

Bragg refraction phenomenon is often used to determine the thickness and/or refractive index of thin films (see Refs. 5 through 7). The technique employed for the present tests, however, was somewhat different than ordinarily used.

For these experiments the angle of incidence, $\beta_i$, was set to some desired value, and the detector arm rotated to the angle of specular reflection ($\beta_r$) and left in that position. Then, the chamber pressure was adjusted to the desired value, the chamber valved off from the pumping system, and the cryosurface cooled with $LN_2$. Carbon dioxide was then bled into the chamber, and the variation of the intensity of the reflected light was monitored continuously. Referring again to Fig. 2, rays IF and AK alternately are in and out of phase as the film thickness grows

and the detector set at $\beta_r$ experiences a varying signal* such as shown in Figs. 14 and 15. A summary of the test conditions for a few of the Bragg experiments is given below.

| Figure | Wavelength $\lambda, \mu$ | $CO_2$ Addition Rate, $cm^3/sec$ | Pressure Level, torr | Cryosurface Area, $cm^2$ | $\beta_i$, deg |
|---|---|---|---|---|---|
| 14a | 0.7 | $1.26 \times 10^{-1}$ | $1 \times 10^{-4}$ | 63 | 25 & 45 |
| 14b | 0.8 | | $1 \times 10^{-4}$ | 63 | 25 & 45 |
| 14c | 0.9 | | $1 \times 10^{-4}$ | 63 | 25 & 45 |
| 15a | 0.9 | | $4.1 \times 10^{-4}$ | 63 | 15 & 35 |
| 15b | 0.9 | | $2.1 \times 10^{-2}$ | 63 | 10 & 25 |
| 15c | 0.9 | | $2.4 \times 10^{-1}$ | 63 | 27 |

If there is no deposit on the cryosurface before the gas is introduced into the chamber, the first peak occurs when q = 1, that is, when the two optical path lengths ($\mu \ell_{AHI}$ and $\ell_{AK}$) differ by one wavelength. The second peak corresponds to q = 2, the third to q = 3, etc. Thus, the change in cryodeposit thickness between two adjacent peaks is

$$\Delta r = \frac{\Delta q \lambda}{2\mu \sqrt{1 - \frac{\sin^2 \beta_i}{\mu^2}}} \tag{12}$$

where $\Delta q \equiv 1$. Because the gas addition rate to the chamber is essentially constant, the cryodeposit grows at a constant rate;

$$\frac{dr}{dt} = \text{constant} = K \tag{13}$$

*This effect was first observed for cryodeposits by Wood et al. (Ref. 1).

This is demonstrated by an essentially constant spacing between adjacent peaks or valleys in the test results shown in Figs. 14 and 15. Equation (12) may be written as

$$K\Delta t = \frac{\lambda}{2\mu\sqrt{1 - \frac{\sin^2\beta_i}{\mu^2}}} \tag{14}$$

where $\Delta t$ is the time interval between adjacent peaks or valleys (see Fig. 14b). When the experiment is conducted at two angles of incidence, $\beta_{i_1}$ and $\beta_{i_2}$, and the detector placed at the two corresponding angles of specular reflection, Eq. (14) may be applied to show that

$$\Delta t_1\sqrt{\mu^2 - \sin^2\beta_{i_1}} = \Delta t_2\sqrt{\mu^2 - \sin^2\beta_{i_2}} \tag{15}$$

Thus, the index of refraction may be calculated from:

$$\mu = \sqrt{\frac{\sin^2\beta_{i_2} - \left(\frac{\Delta t_1}{\Delta t_2}\right)^2 \sin^2\beta_{i_1}}{1 - \left(\frac{\Delta t_1}{\Delta t_2}\right)^2}} \tag{16}$$

with the values of $\Delta t_1$ and $\Delta t_2$ determined from data like those presented in Figs. 14 or 15 at angles $\beta_{i_1}$ and $\beta_{i_2}$, respectively. Equation (16) requires that the gas addition rate be constant and the wavelength be the same for both incidence angles.

### 4.3 ADDITIONAL TESTS

Most of the experimental tests were conducted on $CO_2$ cryofrost films with a xenon light source and a polished copper substrate. In addition, some scattering and Bragg refraction patterns have been obtained with (1) a He-Ne laser light source ($\lambda$ = 6328Å) and (2) a black painted surface. Also, a few tests were conducted on frost films of $H_2O$ and Dow-Corning® 704 diffusion pump oil. The experimental procedures were essentially identical to those described in Sections 4.1 and 4.2.

# SECTION V
# DISCUSSION

## 5.1 REFRACTIVE INDEX MEASUREMENT

Values obtained for the refractive index of $CO_2$ cryodeposits from Eq. (16) and test data like those given in Figs. 14 and 15 are presented in Fig. 16. The cryodeposits were formed over a wide range of pressures. There appears to be little variation of refractive index with pressure, which suggests that the cryodeposit structure is not drastically different when formed at any pressure between about 10 and $10^{-4}$ torr. All of the $CO_2$ frost films were formed on a 77°K surface. Calculated values of the refractive index at a pressure of about $8 \times 10^{-5}$ torr are crossplotted as a function of wavelength in Fig. 17. The present test results agree reasonably well with a value obtained by an interference fringe method at $\lambda = 1.1\ \mu$ by Yamada and Person (Ref. 8). Refractive indices shown in Fig. 17 have been used in all subsequent calculations.

## 5.2 VERIFICATION OF SCATTERING THEORY

If the substrate reflects only a small portion of the light that strikes it, the intensity of the reflected t-family rays (Fig. 2) would be greatly reduced which in turn would reduce the intensity of the re-emitted s-family of rays. This should result in much more pronounced Bragg interference patterns as ray AK which is unchanged goes in and out of phase with ray IF whose intensity would be significantly reduced. Also, reducing the intensity of the emerging scattered s-families should greatly reduce the magnitude of any interference peaks attributable to scattering. To determine if this was the case, carbon dioxide cryodeposits were formed on a substrate which was coated with a black epoxy paint. Typical results from one of these tests are given in Figs. 18 and 19.

Bragg refraction data (Fig. 18) demonstrated that the amount of light reflected by a $CO_2$ film on the black substrate was about two orders of magnitude lower than when a copper substrate was used (Figs. 14 or 15). However, the signal difference between peaks and valleys as the $CO_2$ deposit grew on the black substrate was approximately 50 percent of the overall signal level, whereas with the copper substrate this difference was only 10 percent of the signal level. Thus, reducing the reflectivity of the substrate produced much more pronounced Bragg interference as

expected. Secondly, as shown in Fig. 19, the distribution of reflected light from a thin cryodeposit on a black substrate showed no detectable evidence of scattering interference patterns. Consequently, the effects of a black substrate were consistent with the proposed scattering model.

The validity of the proposed simple scattering theory can be further determined by computation of the cryodeposit thickness from Eqs. (5) and (8), or Eqs. (9) and (10) if the light is normal to the surface. If the scattering model is correct, Eqs. (9) or (10) should predict a single thickness for all of the values of $\beta_n$ at which peaks occur in Fig. 12, for example, and for all four wavelengths. As an illustration, the various peaks of one interference pattern in Fig. 12 are identified by the particular sets of integers which satisfy Eqs. (9) and (10).

A comparison of the thickness predicted by Eqs. (9) and (10) is given in Fig. 20. In this case the incident beam was normal to the surface, and both types of interference are observed to produce the same result. That is, the interference of ray CL with AD and ray CL with IJ produce constructive interference peaks which are superimposed upon each other at the nearly same values of $\beta_n$. As will be shown later, this only occurs for normal incidence. The variation shown by the solid boxes in Fig. 20 represents at each thickness perhaps 30 to 40 separate calculations of $\tau$. The variation in the calculated values of $\tau$ is probably within the accuracy of reading $\beta_n$ for each peak from the distribution record. Alternately, the scattering theory proposed in Section II allows one to predict the angular positions of the interference peaks or valleys. Figure 21 contains a comparison of calculated and measured angles at which interference peaks occur. In this instance, the $CO_2$ film thickness was computed from the angular position of one pronounced peak; and, then using that thickness, the angular positions of the remaining observable peaks and valleys were calculated for a number of tests. Again, good agreement between the measured and calculated values is evident.

After the Bragg refraction data were obtained and the $CO_2$ flow terminated, scattering patterns were often recorded for the resulting cryodeposit layer. This allowed direct comparisons of cryodeposit thickness determined by two independent methods:

1. From the Bragg interference data (Figs. 14 and 15) and Eq. (11), where q = 1 for the first peak after the flow is initiated; q = 2 for the second and so on; and,

2. From the scattering interference data and Eqs. (9) and (10)

The first is a transient measurement of thickness as the cryodeposit grows on the substrate, whereas the thickness determined from the

scattering interference data is a steady-state measurement on a given deposit. Deposit thicknesses, determined from Eq. (11) and data similar to that given in Fig. 14, are shown by the circles in Fig. 22 and are compared to the thicknesses of cryodeposits formed at essentially the same conditions but determined from Eqs. (9) and (10). Results obtained from the proposed scattering theory are seen to agree quite well with thicknesses given by the Bragg Equation.

Scattering interference patterns have also been measured when the incident beam is at some angle $\beta_i$ other than normal (Fig. 13) and a comparison of the calculated thickness for $\beta_i = 0$ deg and $\beta_i \neq 0$ serves to illustrate which type of scattering interference is predominant. The interference patterns presented in Figs. 12 and 13 were measured for the same cryodeposit, but with $\beta_i = 0$ deg and $\beta_i = 21.5$ deg, respectively. Also, Bragg interference data were obtained as this layer was deposited and indicated that the layer was $13.37\mu$ thick when the data given in Figs. 12 and 13 were taken. The results of calculations of $\tau$ from the scattering theory equations are compared in the table below for this particular test.

| Fig. 12 Data, $\beta_i = 0$ deg | | | | Fig. 13 Data, $\beta_i = 21.5$ deg | | | |
|---|---|---|---|---|---|---|---|
| Eq. (9) | | Eq. (10) | | Eq. (5) | | Eq. (8) | |
| m | $\tau$ | n | $\tau$ | m | $\tau$ | n | $\tau$ |
| 33 | 13.15 | 1 | 12.68 | 37 | 13.68 | 1 | 32.29 |
| 32 | 13.50 | 2 | 12.10 | 36 | 13.42 | 2 | 30.21 |
| 31 | 13.01 | 3 | 12.41 | 35 | 13.41 | 3 | 29.23 |
| 30 | 13.65 | 4 | 12.95 | 34 | 13.40 | 4 | 28.11 |
| 29 | 13.61 | 5 | 13.25 | 33 | 13.42 | 5 | 26.46 |
| 28 | 13.43 | 6 | 13.11 | 32 | 13.48 | 6 | 25.82 |

It is clear that Eq. (5) predicts the cryodeposit thickness when $\beta_i \neq 0$, whereas Eq. (8) doesn't. Thus, it appears that the interference between the refracted rays in the s-families and r-family rays at the same angle is much more pronounced than the other interference mode considered. Additional calculations with data obtained at two angles of incidence (Fig. 23) indicate Eq. (5) properly predicts the cryodeposit thickness with relatively small scatter over a range of thicknesses.

All of the above comparisons demonstrate rather conclusively that Eq. (5) or (9) can be used to determine simply and accurately the thickness of a cryodeposit from measured interference patterns. Consequently, it is believed that light is primarily scattered by the cryodeposit surface, and the scattering and interference mechanism must closely follow the model proposed prior to the development of Eq. (5).

### 5.3 THICKNESS MEASUREMENTS

The previous section has demonstrated that the proposed scattering model allows accurate calculation of cryodeposit film thickness. The thicknesses of cryodeposits formed over a wide range of conditions have been determined from Eqs. (5) or (9), and the results of a number of these calculations are given in Figs. 22 through 25. In every case, there was only a small variation in the thickness determined from the various angular locations of all peaks and valleys and for the four wavelengths used. Scatter bands are used in these figures to illustrate the amount of variation. Deposit thickness up to $100\mu$ have been determined by this method.

Straight lines have been put through the data points in Figs. 24 and 25 which indicate that over a range of thickness from about 5 to $35\mu$, the cryodeposit growth rate is constant. At thicknesses below about $5\mu$, the first interference peaks occurred at relatively large angles where the intensity was too low to discern the peak. As the layer thickened, the scattering interference peaks continuously shifted to lower angles and moved closer together. At a thickness of about $100\mu$, the interference peaks could no longer be resolved because they began to overlap with each other and with the specular peak. This thickness measurement technique could be extended by use of truly monochromatic light of shorter wavelengths when the layers are thin and of much longer wavelengths for thick layers.

It may also be observed in Figs. 23 through 25 that the linear variation of the cryodeposit growth does not extrapolate to the origin. Cryodeposit thicknesses in the range 0 to $5\mu$ can be determined from Eq. (11). As shown in Fig. 22, the Bragg interference data indicate the same trend for the cryodeposit growth. It is not known if this trend is attributable to the dynamics of the gas addition system or is some basic characteristic of cryodeposit formation.

## 5.4 DENSITY MEASUREMENTS

The mean density of a thin cryodeposit can also be estimated from the thickness measurements. If the chamber pressure is constant as gas is being admitted, then the gas is being cryopumped at the same rate as it is flowing into the chamber. Thus, conservation of mass requires

$$\dot{m}_a = \dot{m}_c$$

or

$$\frac{P_f \frac{dV_s}{dt}}{RT} = \bar{\rho}_c \int_{A_s} \frac{dr(A)}{dt} dA$$

If we assume that the cryodeposits growth rate is uniform over the cryosurface, then

$$\bar{\rho}_c = \frac{P_f}{RTA_s} \left(\frac{dV_s}{dr}\right) \tag{17}$$

Thus, the density of the cryodeposit is inversely proportional to the slope of the curves given in Figs. 22 through 25.

For one set of tests, the cryosurface was surrounded by a box in such manner that the $CO_2$ frost could only form on a portion of the irradiated surface. Cryodeposit densities have been obtained from Eq. (17) for this particular set of tests and are shown in Fig. 26. They are presented as a function of the pressure level at which they were formed where helium was essentially the background gas. The density of $CO_2$ cryodeposits increases from about 1.3 gm/cc to about 1.7 gm/cc as the pressure under which the deposit is formed increases from $10^{-4}$ to 1 torr. The present estimates of density extrapolate reasonably well to the range of densities given for dry ice. The variation of density with pressure is consistent with that predicted by the thermodynamics of a pure substance. The accuracy of the present values, however, depends upon the uniformity of the cryodeposit thickness. The light spot covers about a 2-cm-diam circle, and the thickness measurement represents a mean value over that area. The light spot was moved to different locations over the cryodeposit, and essentially the same thicknesses were measured. It is believed that the values shown in Fig. 26 are probably accurate to ±0.1 gm/cc.

## 5.5 MEASUREMENTS ON OTHER TYPES OF FILMS

Other types of cryodeposits were also found to produce scattering and Bragg interference patterns. Figure 27 compares the angular

distribution of light from a bare polished copper surface with two distributions obtained from thin $H_2O$ cryodeposits formed on a 77°K surface. Scattering interference peaks were observable but were not nearly as pronounced as those previously presented for a $CO_2$ cryodeposit (Fig. 13). Similar effects were also observed (Fig. 28) when Dow-Corning 704® diffusion pump oil was intentionally introduced into the test chamber and frozen onto a 77°K surface. Only a few data were taken in these two cases, but they clearly indicated the proposed scattering model and thickness measurement technique would be applicable to other cryodeposits. In both cases the experimental apparatus did not allow careful control and accurate measurement of the water or pump oil into the chamber. Consequently, it was not possible to determine the refractive indices and densities of these two substances. However, the scattering and Bragg interference phenomena exist and such measurements are possible with the proper flowmetering equipment.

Measurements of the angular distribution of light reflected from a liquid oil film and two mechanical films (20-$\mu$ cellophane and a 40-$\mu$ photographic film with the emulsion removed) did not result in any interference patterns. Thus, one might conjecture that these films do not scatter light like the cryodeposits and that the scattering phenomena may be related to the unique character of the surface of the cryodeposit.

### 5.6 MEASUREMENTS WITH A LASER LIGHT SOURCE

Some scattering interference patterns were measured utilizing laser light at a wavelength of 6328 Å as the radiation source. Figure 29 contains the resulting scattering patterns for the beam directed normal to the surface and at an angle of incidence of 18 deg. When these patterns are compared to some of those obtained with filtered light, it is observed that the resolution is greatly improved by use of the laser. Many more peaks may be detected. Trends shown in Figs. 8 through 13 can provide a guide for selecting the wavelength for a monochromatic light source which might be used in any application of these scattering phenomena or measurement technique.

## SECTION VI
## CONCLUSIONS

From the Bragg refraction data obtained for a varying cryodeposit thickness, the following conclusions can be made:

1. The refractive index of carbon dioxide cryodeposits can be easily determined from Bragg refraction patterns when the

deposit thickness is less than 25 $\mu$. The refractive index varied from about 1.45 at a wavelength of 0.6 $\mu$ to 1.38 at 0.9 $\mu$.

2. The density of $CO_2$ cryodeposits formed on a 77°K surface was also obtained from these data and varied between 1.3 and 1.7 gm/cc. The density was found to depend slightly on the chamber pressure at which the deposits were formed, with the density increasing for an increasing chamber pressure.

From the measurement of scattering interference patterns from a cryodeposit of given thickness, the following conclusions can be made:

1. A scattering model has been proposed which quite accurately predicts the thickness of cryodeposit films from observed interference patterns. The basic assumption in the scattering model is that light is significantly scattered by reflection from and/or passage through the surfaces of thin cryodeposits. Further, the predominant scattering mechanism for thin cryodeposits is identified.

2. Deposit thicknesses up to 100 $\mu$ can be determined from the interference maxima and/or minima. A simple equation is derived which may be used to accurately determine film thickness from the measured scattering interference pattern (Eq. (5), Section II).

3. The scattering phenomena occurred for the three types of cryodeposits studied: $CO_2$, $H_2O$, and diffusion pump oil frosts.

4. Use of laser light significantly improves the resolution of interference peaks and accuracy of cryodeposit film thickness measurement.

## REFERENCES


1. Wood, B. E., Smith, A. M., and McCullough, B. A. "The Spectral Reflectance of Water and Carbon Dioxide Cryodeposits from 0.36 to 1.15 Microns." AEDC-TR-67-131, August 1967.

2. McCullough, B. A., Wood, B. E., and Smith, A. M. "A Vacuum Integrating Sphere for In Situ Reflectance Measurements at 77°K from 0.5 to 10 Microns." AEDC-TR-67-10 (AD650072), April 1967.

3. McCullough, B. A., Wood, B. E., and Dawson, J. P. "Thermal Radiative Properties of Carbon Dioxide Cryodeposits from 0.5 to 1.1 Microns." AEDC-TR-65-94 (AD468632), August 1965.

4. Jenkins, Francis A. and White, Harvey E. Fundamentals of Optics. McGraw-Hill Book Company, Inc., 1957.

5. Pliskin W. A. and Conrad, E. E. "Nondestructive Determination of Thickness and Refractive Index of Transparent Films." IBM Journal, January 1964.

6. Pliskin, W. A. and Esen, R. P. "Refractive Index of $SiO_2$ Films Grown on Silicon." Journal of Applied Physics, Vol. 36, No. 6, June 1965, pp. 2011-2013.

7. Hunter, W. R. "High Reflectance Coatings for the Extreme Ultra-Violet." Optica Acta, 1962, pp. 255-268.

8. Yamada, Haruka, and Person, Willis B. "Absolute Infrared Intensities of the Fundamental Absorption Bands in Solid $CO_2$ and $N_2O$." The Journal of Chemical Physics, Vol. 41, No. 8, October 15, 1964, pp. 2478-2487.

# APPENDIXES

I. ILLUSTRATIONS

II. METHODS OF CALCULATION

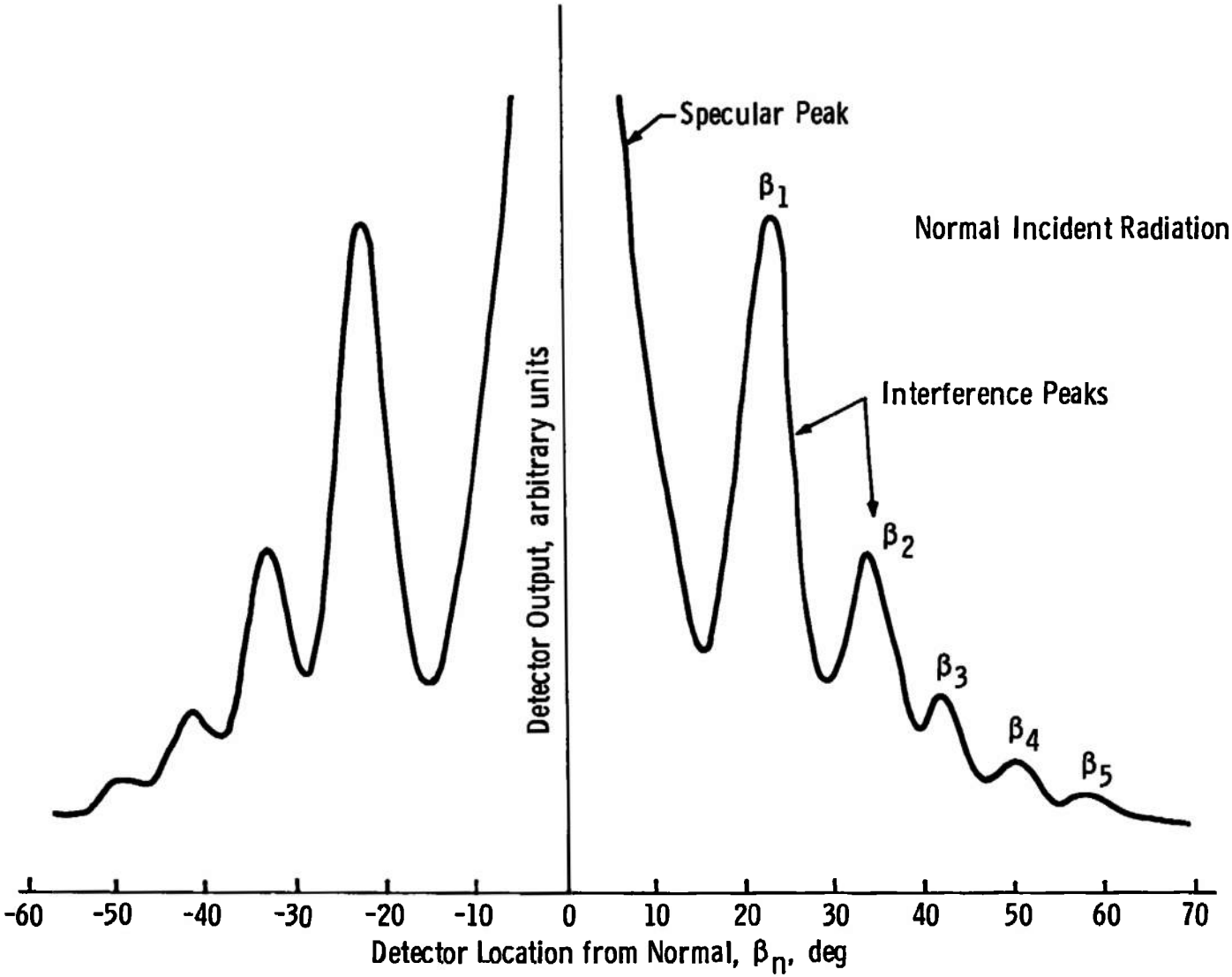


Fig. 1 Typical Interference Scattering Pattern for Thin $CO_2$ Cryodeposits

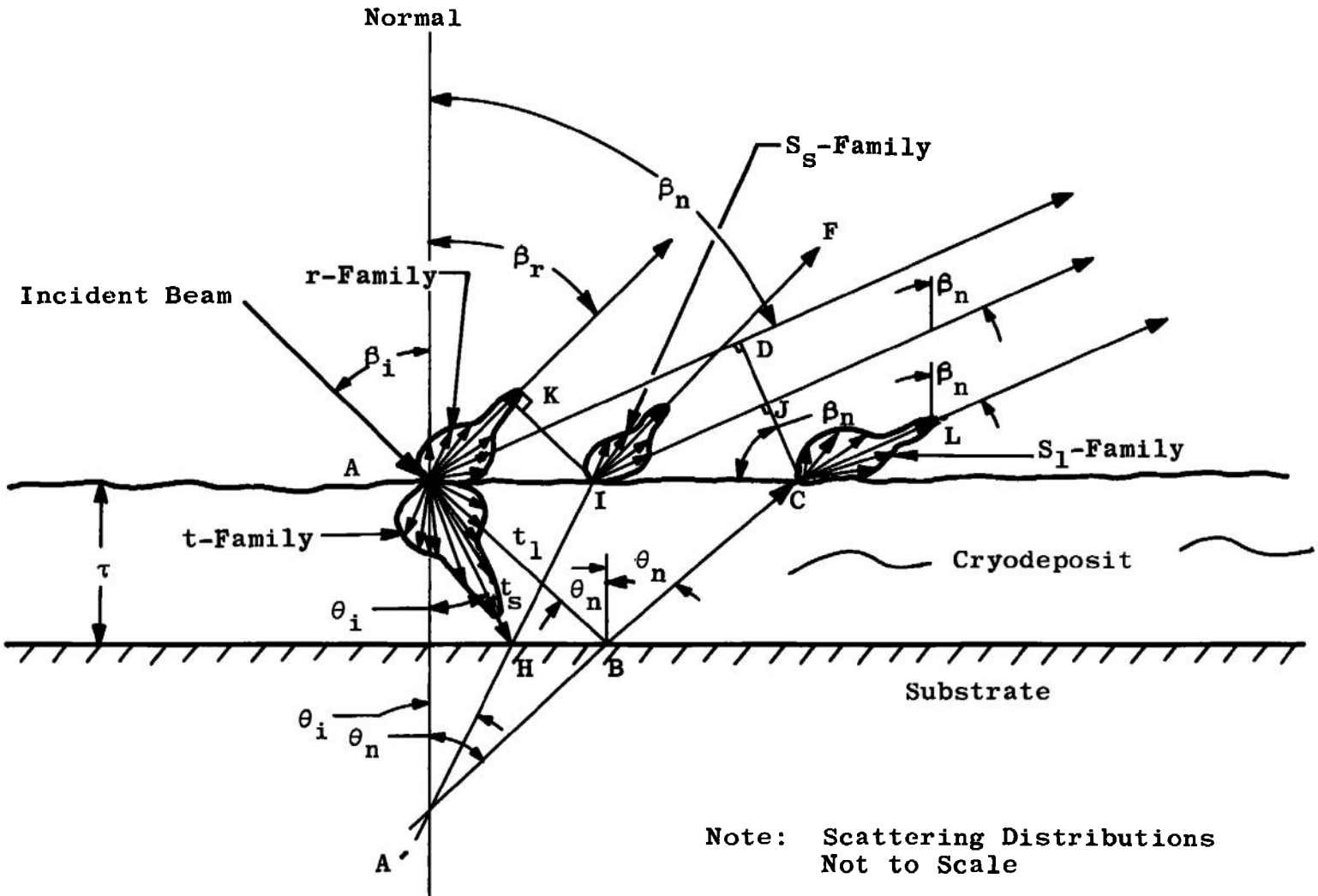


Fig. 2 Schematic of Light Scattering Model

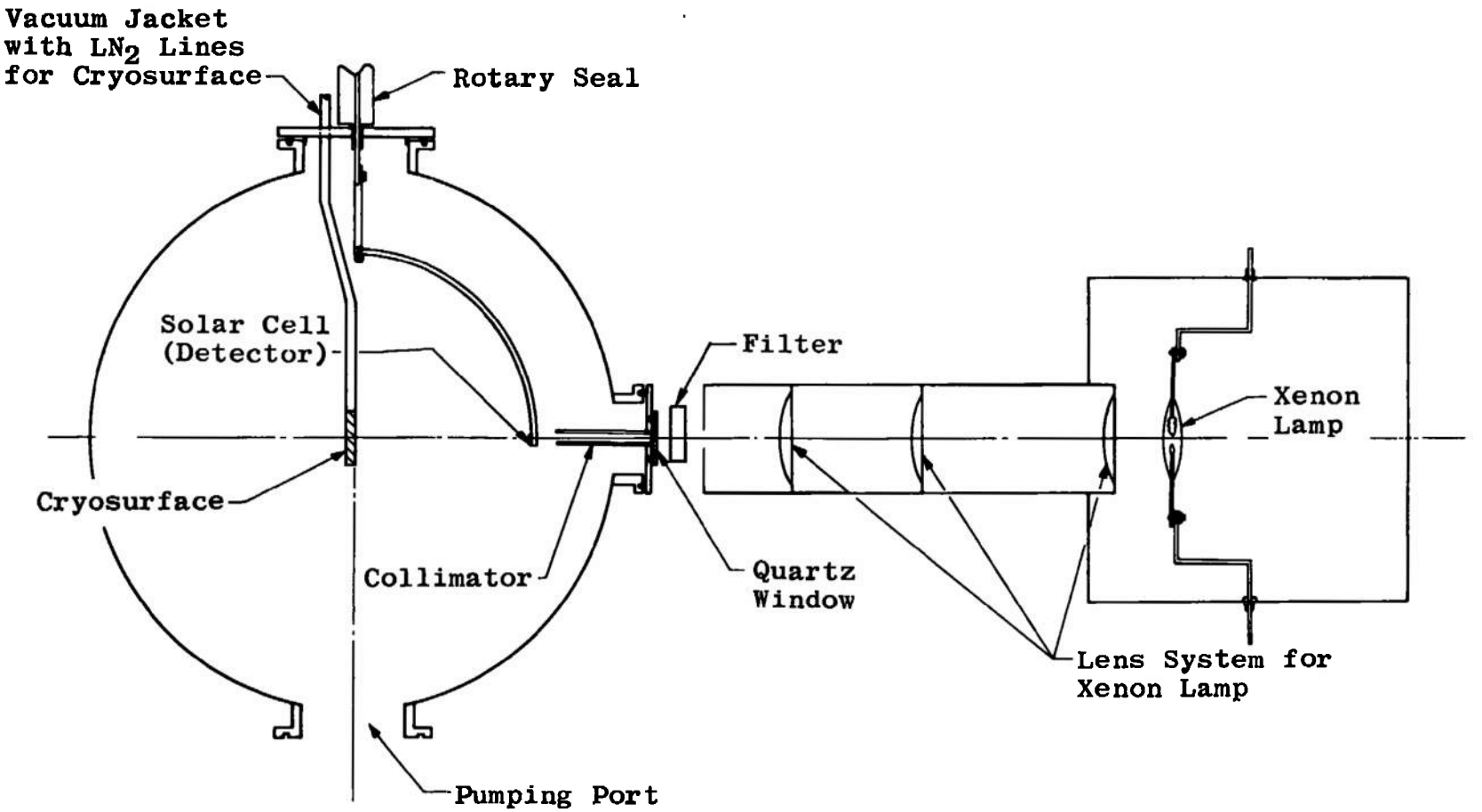


Fig. 3 Schematic of Experimental Apparatus

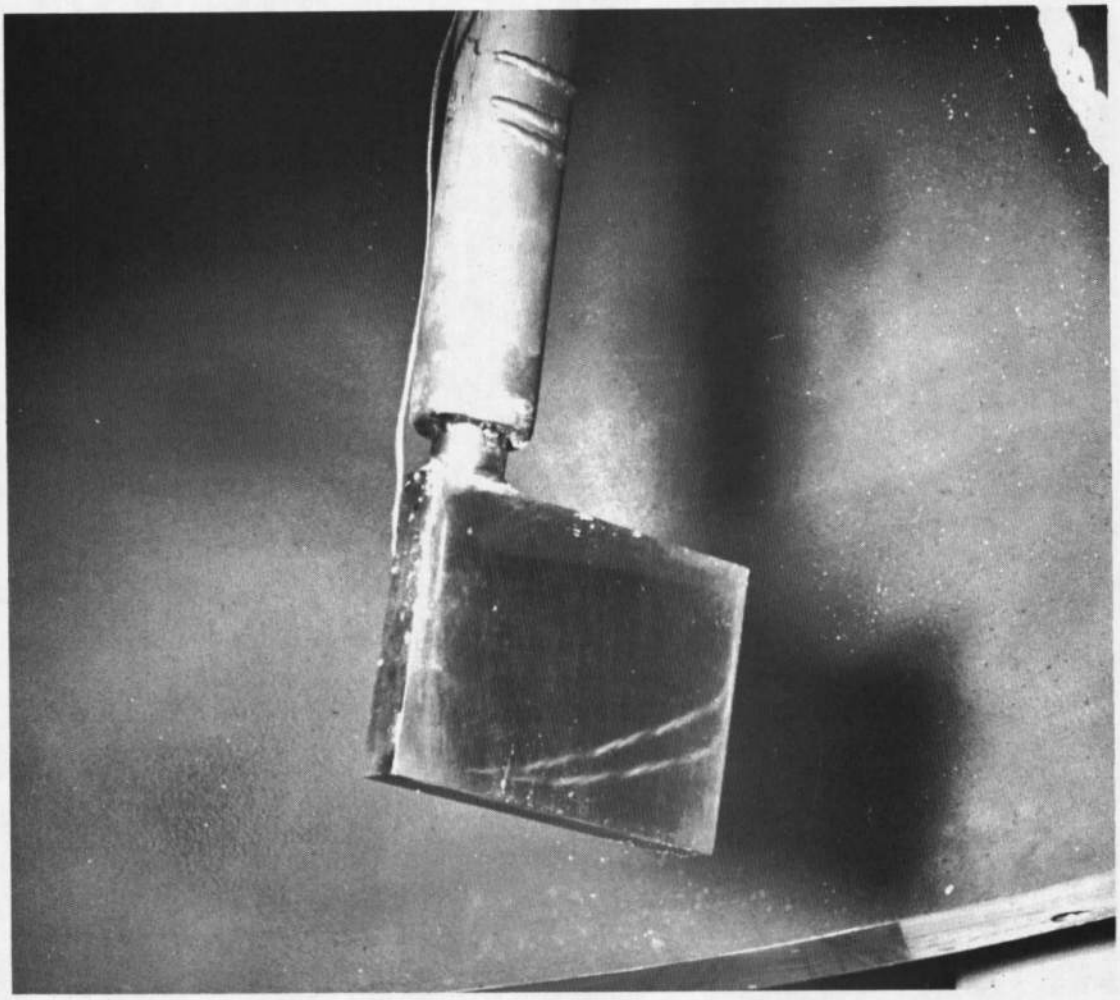

Fig. 4 Photograph of 200-cm$^2$ Polished Copper Cryosurface

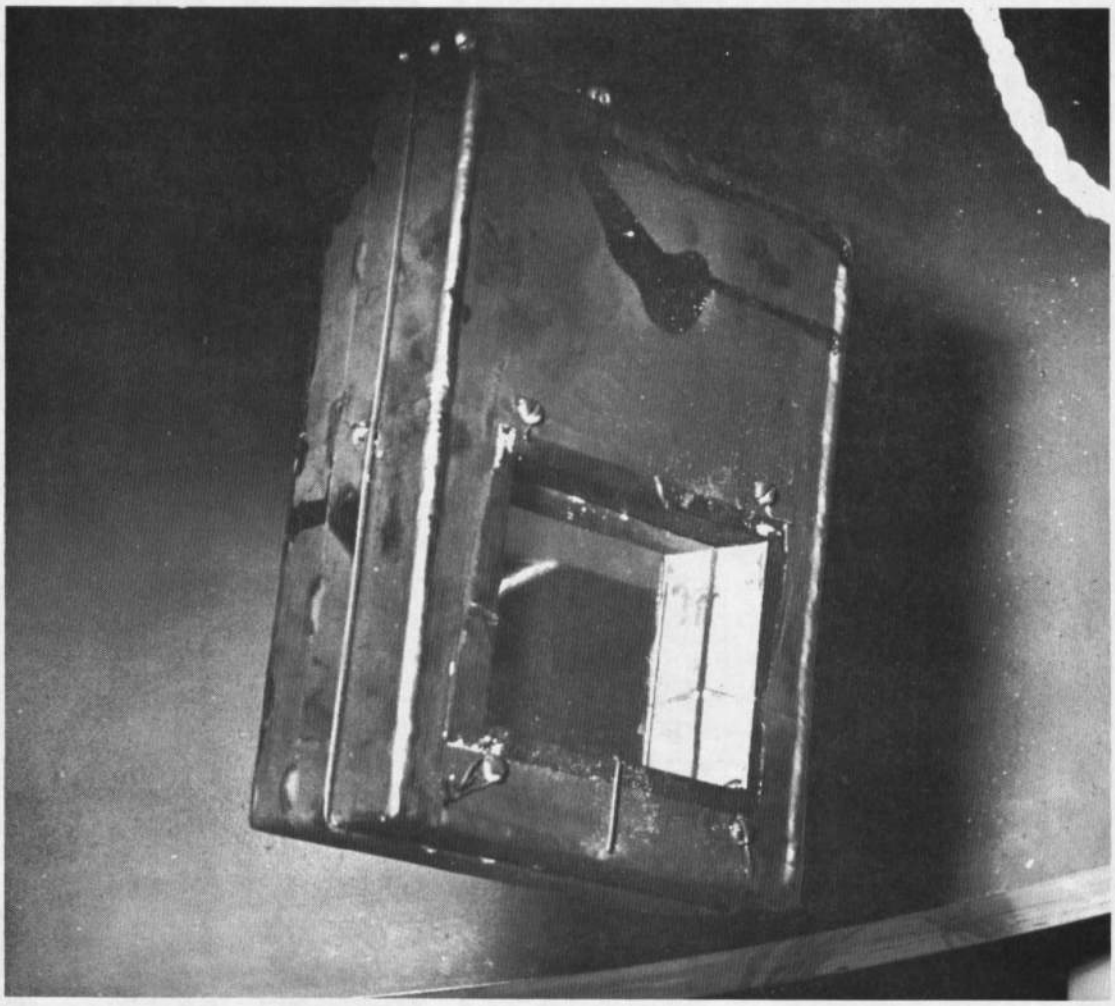

Fig. 5 Photograph of Heating Jacket

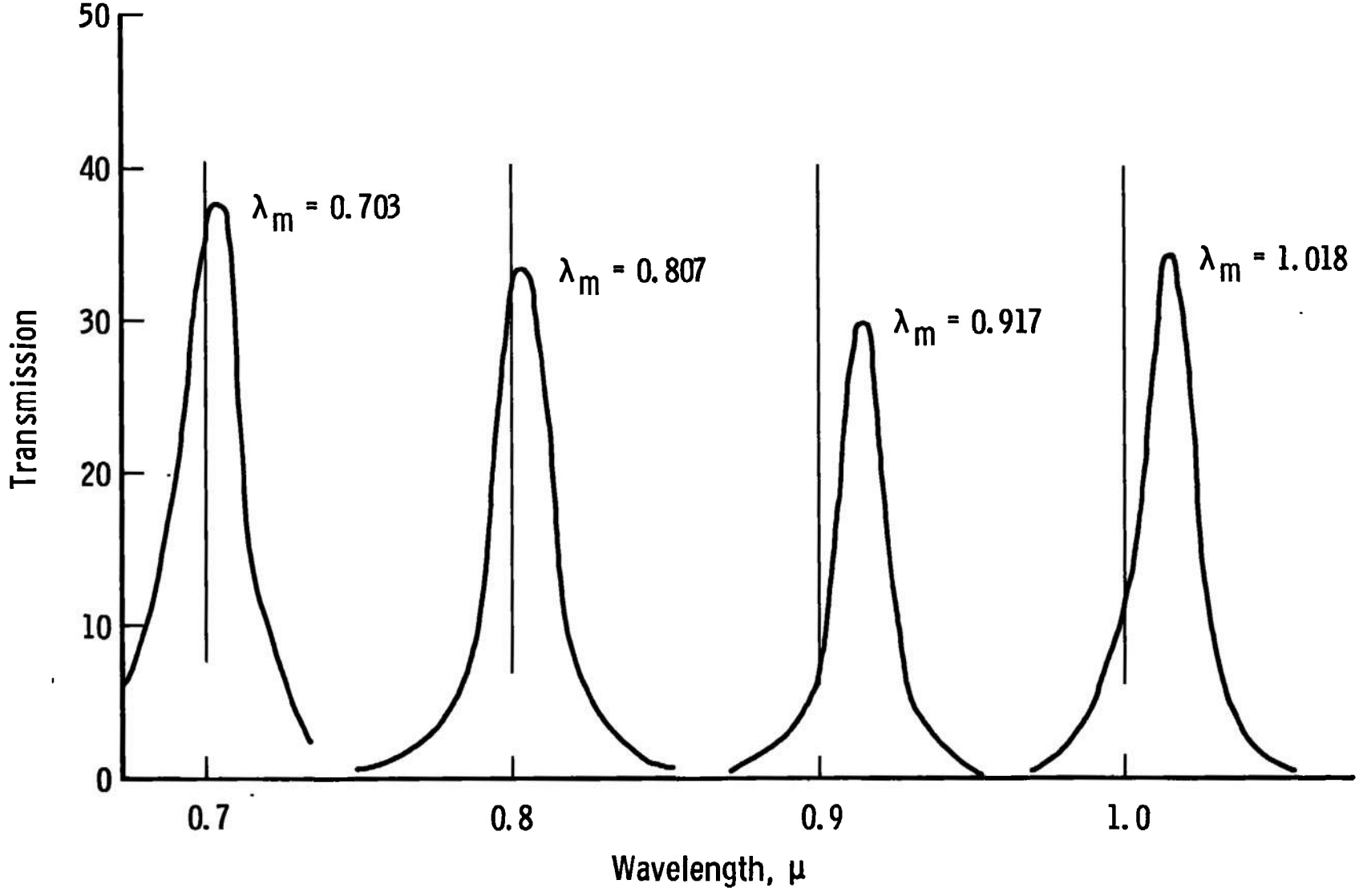


Fig. 6 Filter Transmission Characteristics

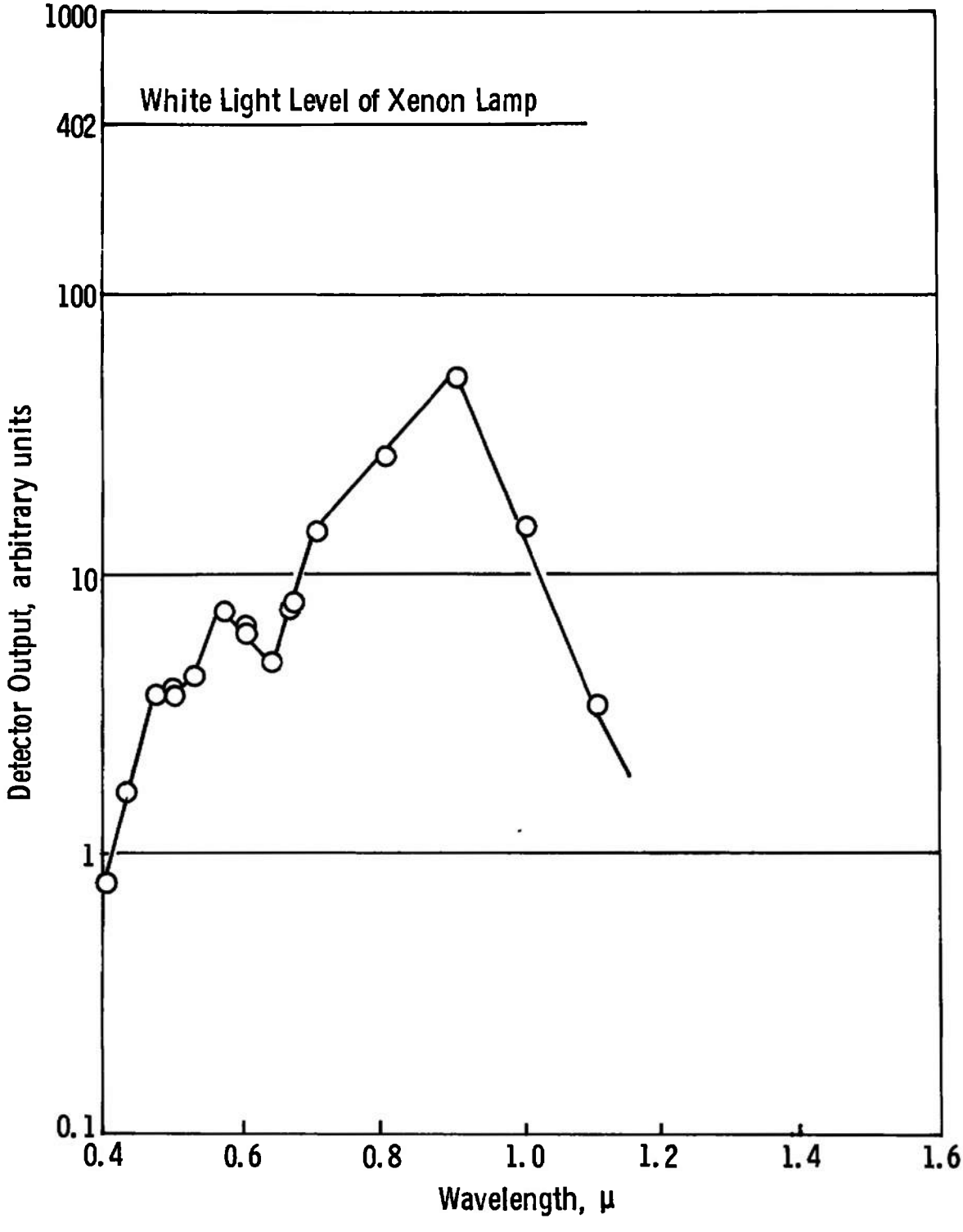


Fig. 7 Detector Output-Wavelength Spectrum of Light Source, Filter, Solar Cell Detector System

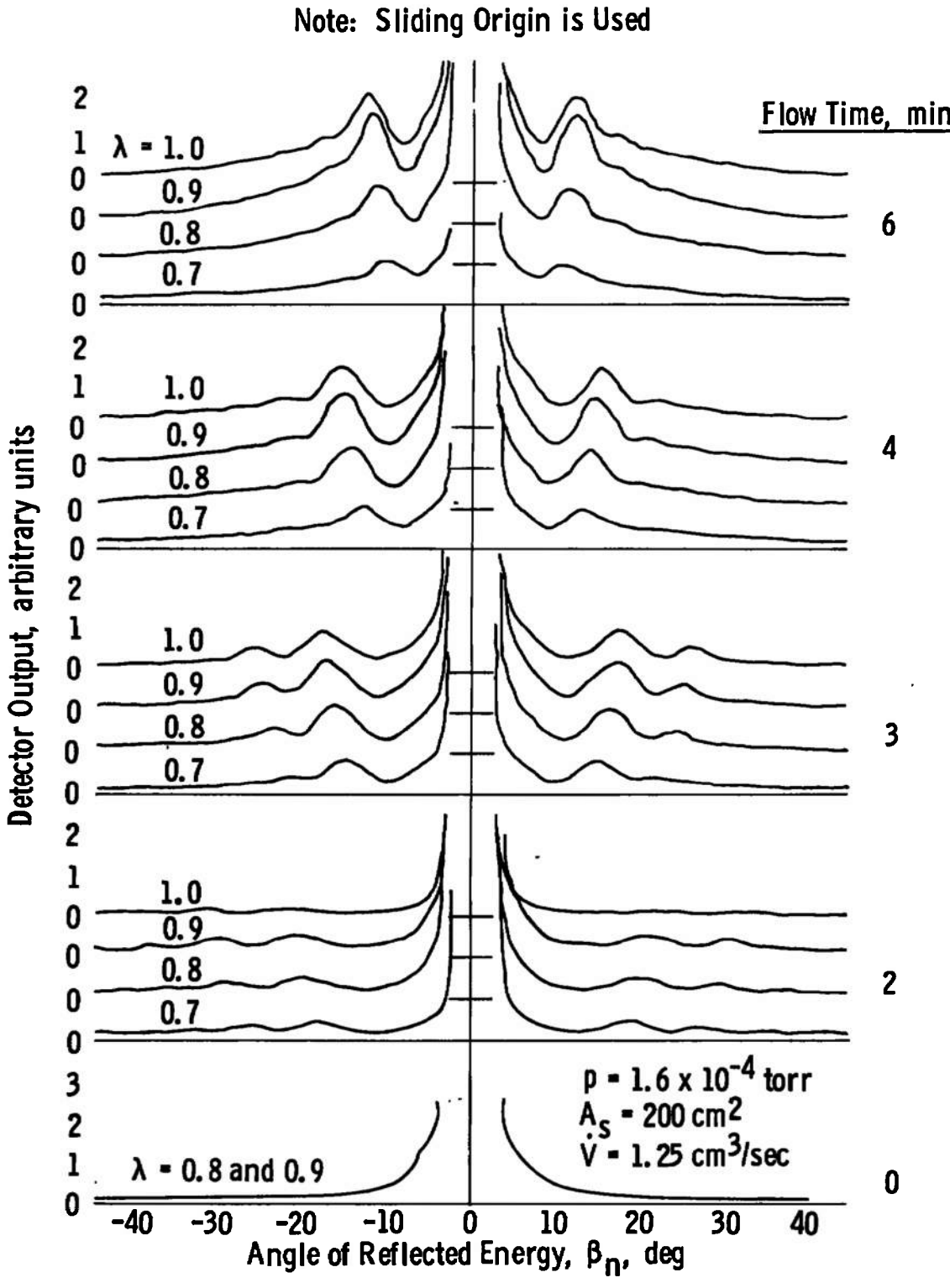


Fig. 8 Scattering Interference Patterns for Normal Incidence and a $CO_2$ Input Rate of 1.25 $cm^3/sec$

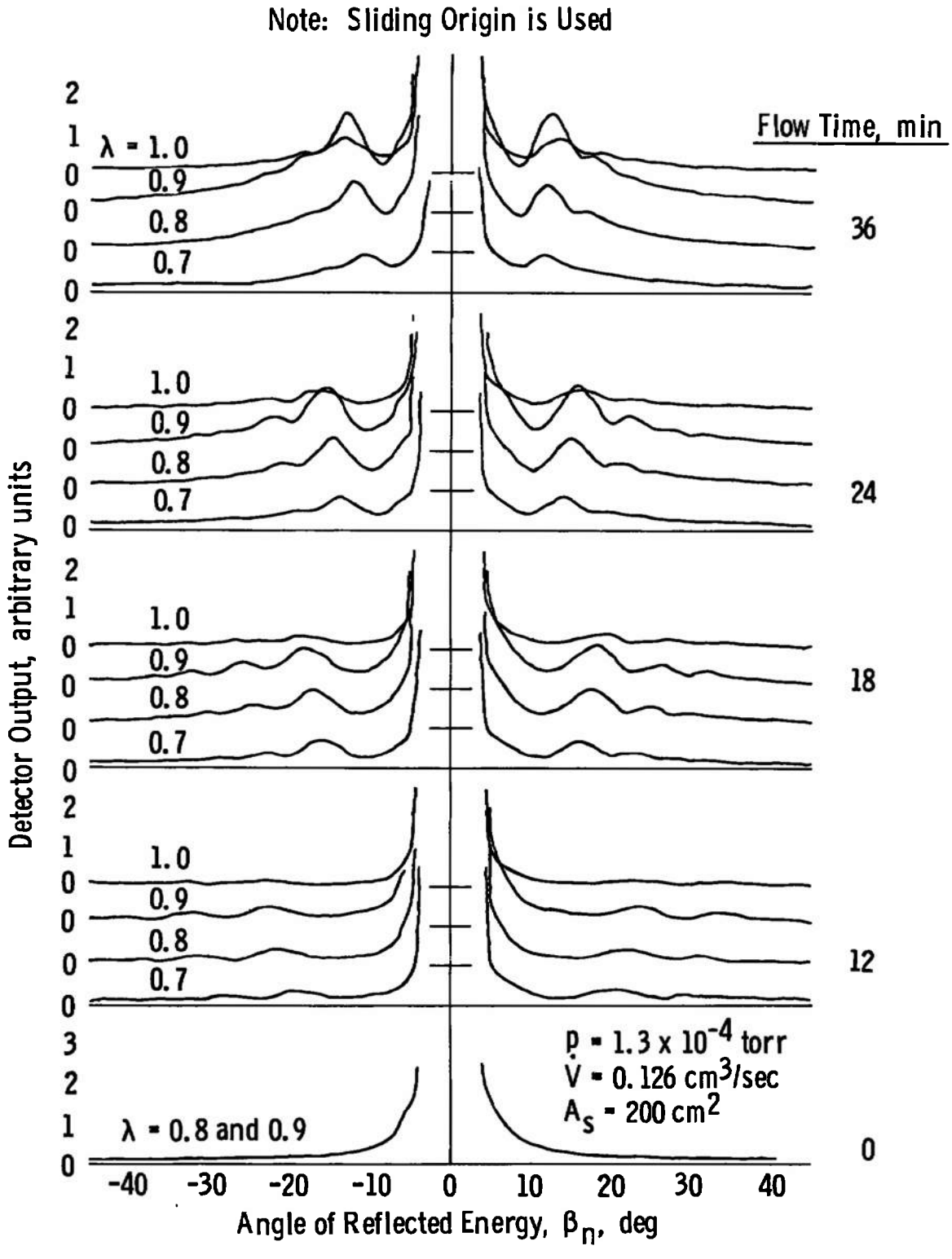


Fig. 9 Scattering Interference Patterns for Normal Incidence and a $CO_2$ Input Rate of 0.126 $cm^3$/sec

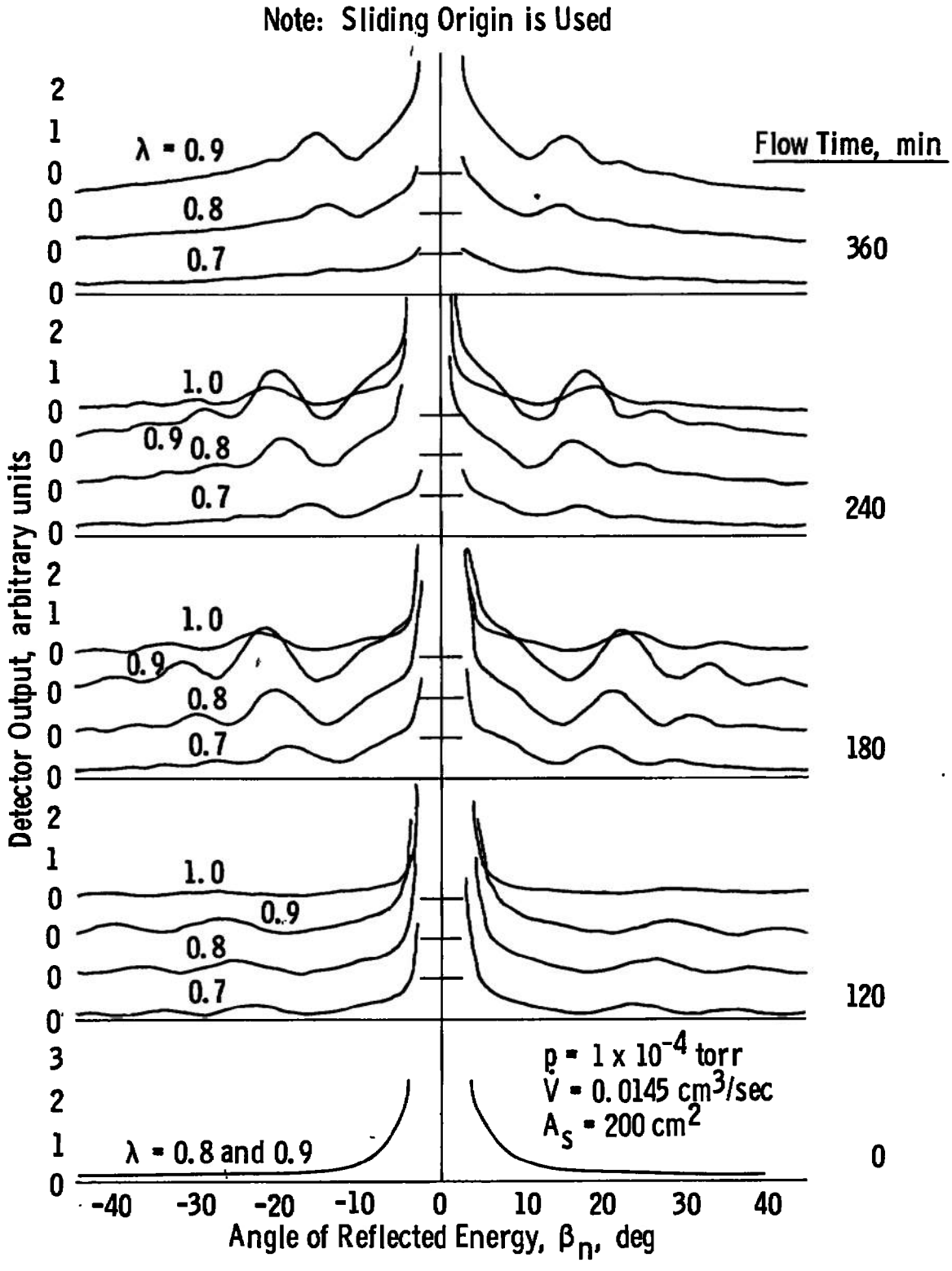


Fig. 10 Scattering Interference Patterns for Normal Incidence and a $CO_2$ Input Rate of 0.0145 $cm^3/sec$

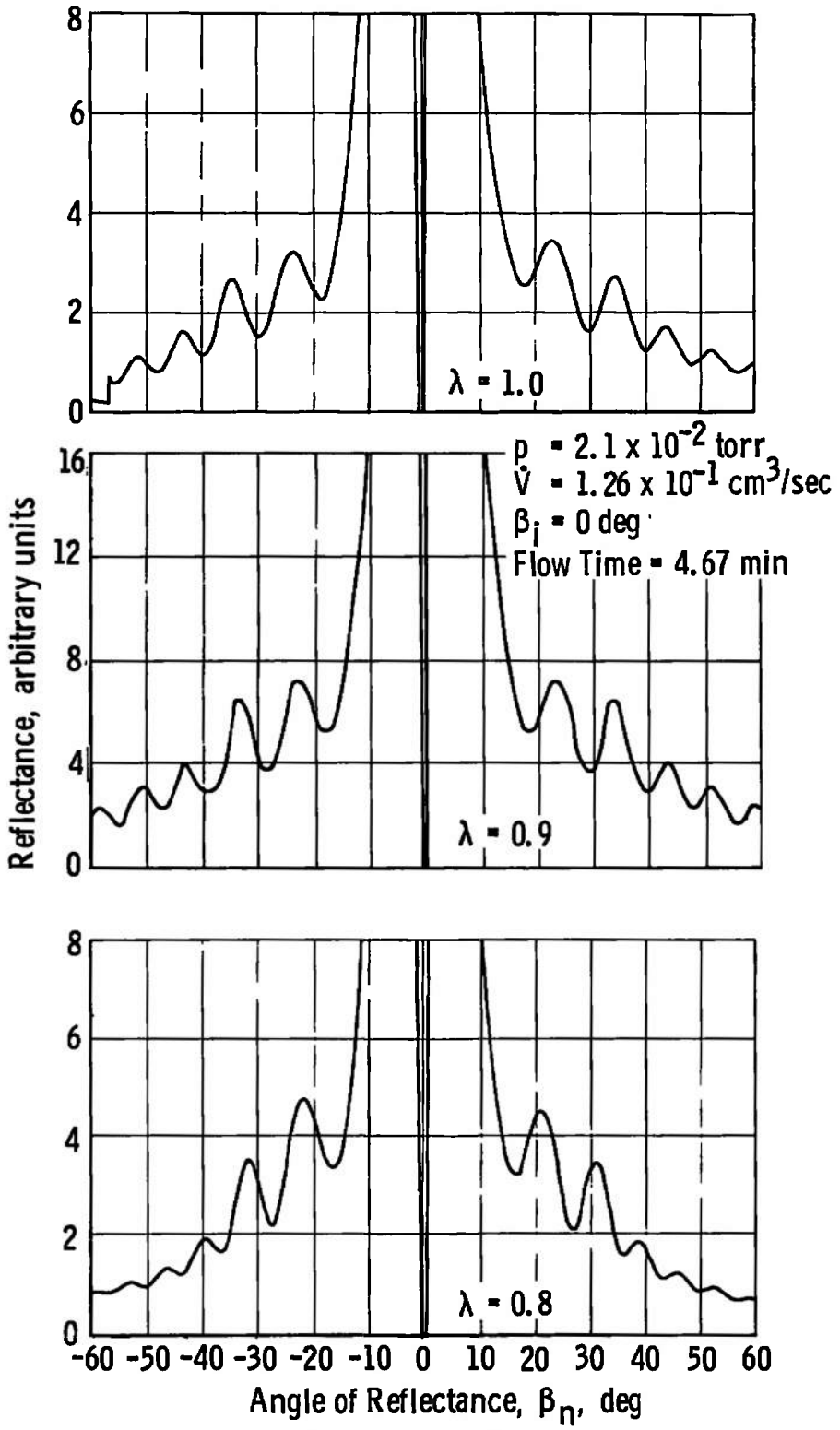


a. Flow Time = 4.67 min

Fig. 11 Effect of Wavelength on Scattering Interference Patterns for $CO_2$ Cryodeposits at $P = 2.1 \times 10^{-2}$ torr

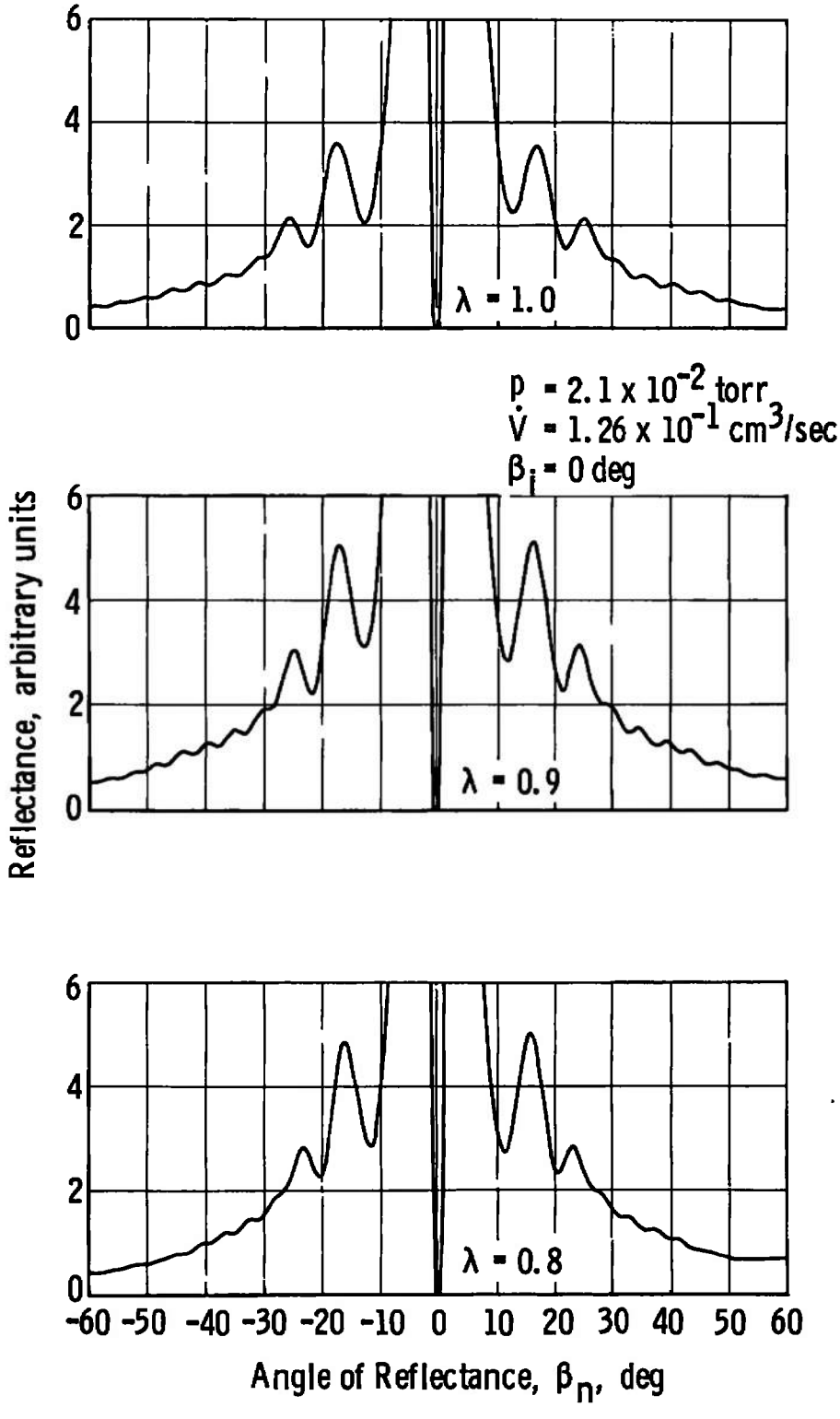


b. Flow Time = 9.5 min

Fig. 11 Concluded

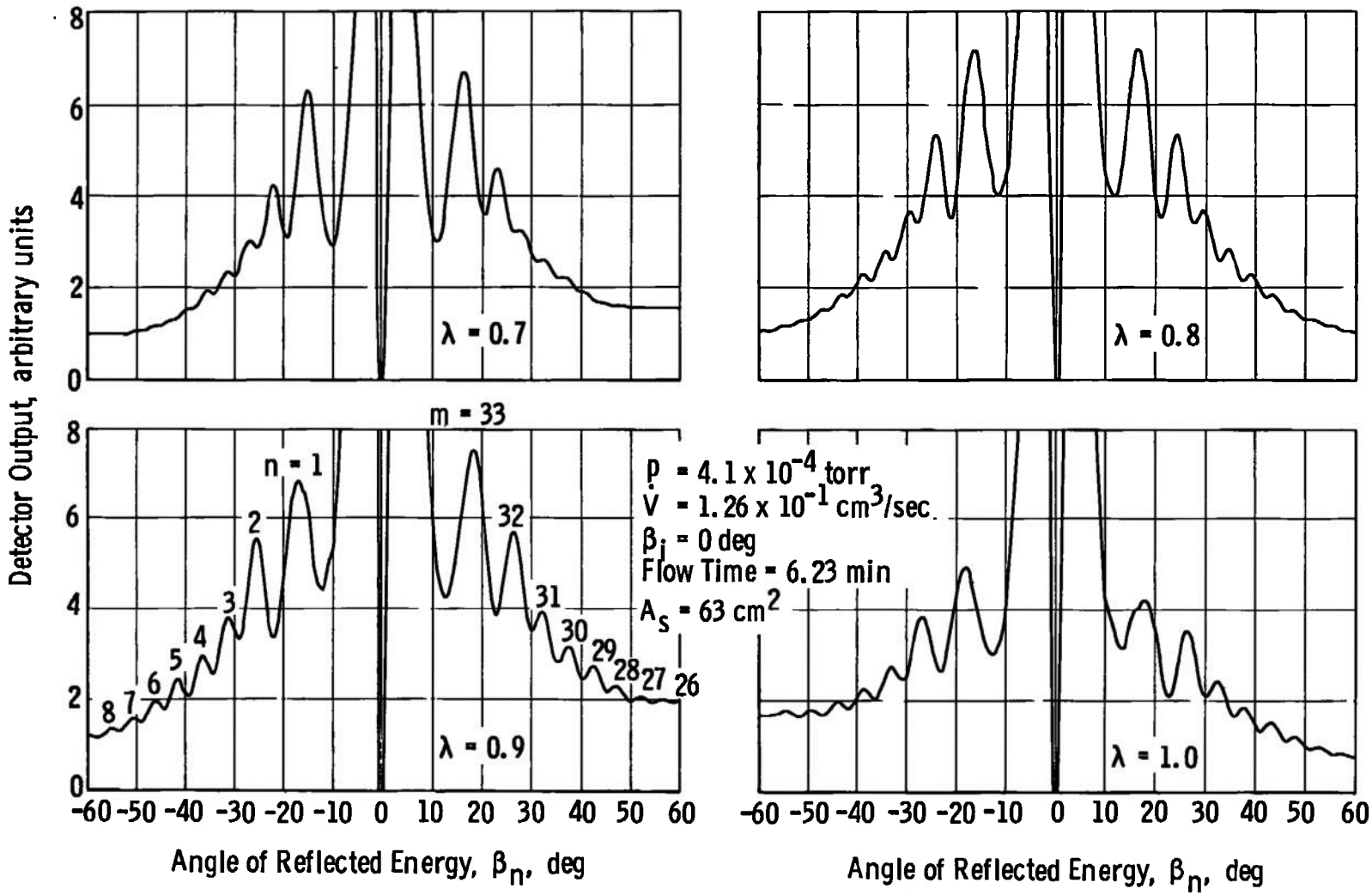


Fig. 12 Effect of Wavelength on Scattering Interference Patterns for $CO_2$ Cryodeposits at $P = 4.1 \times 10^{-4}$ torr

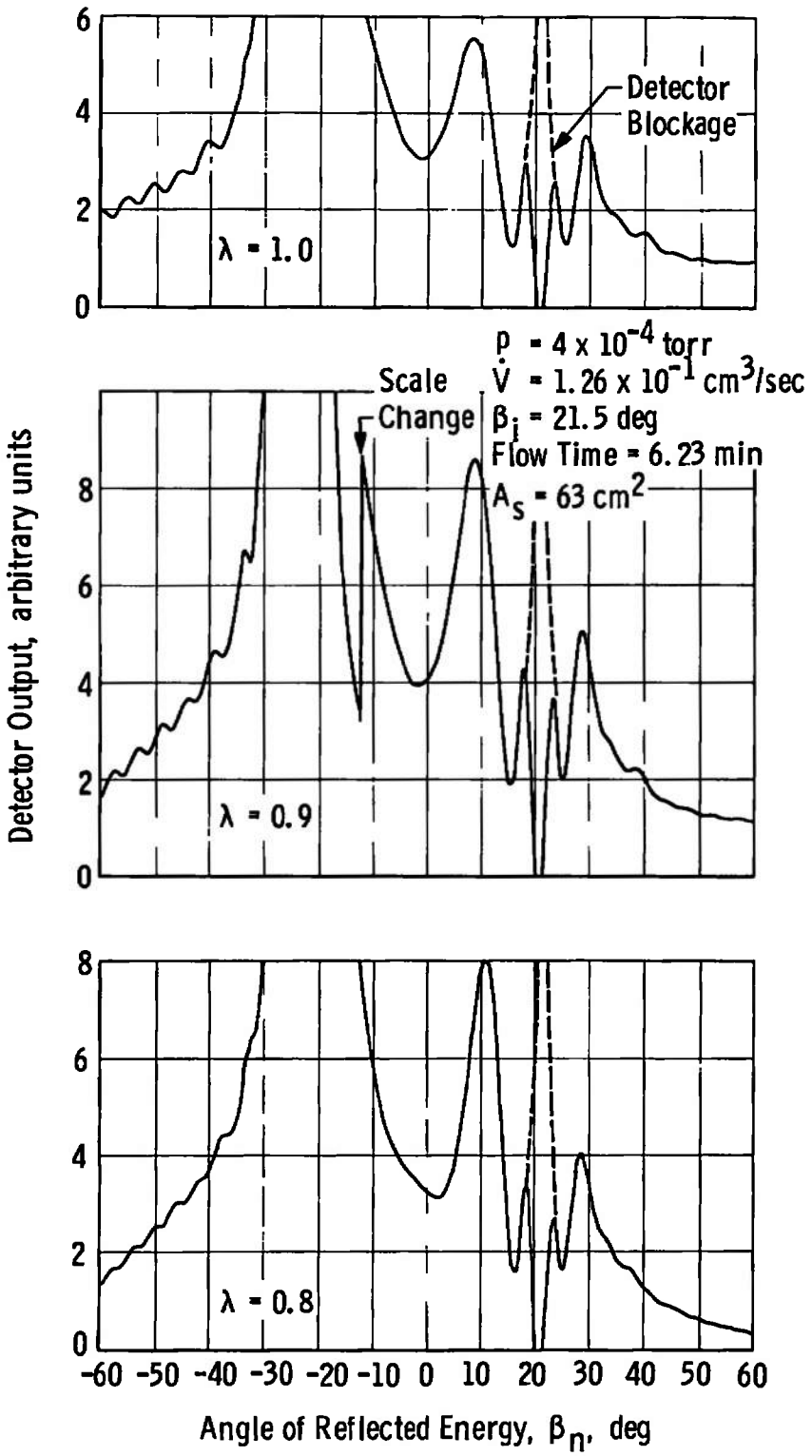


Fig. 13 Scattering Interference Patterns for $CO_2$ Cryodeposits with Nonnormal Incident Radiation

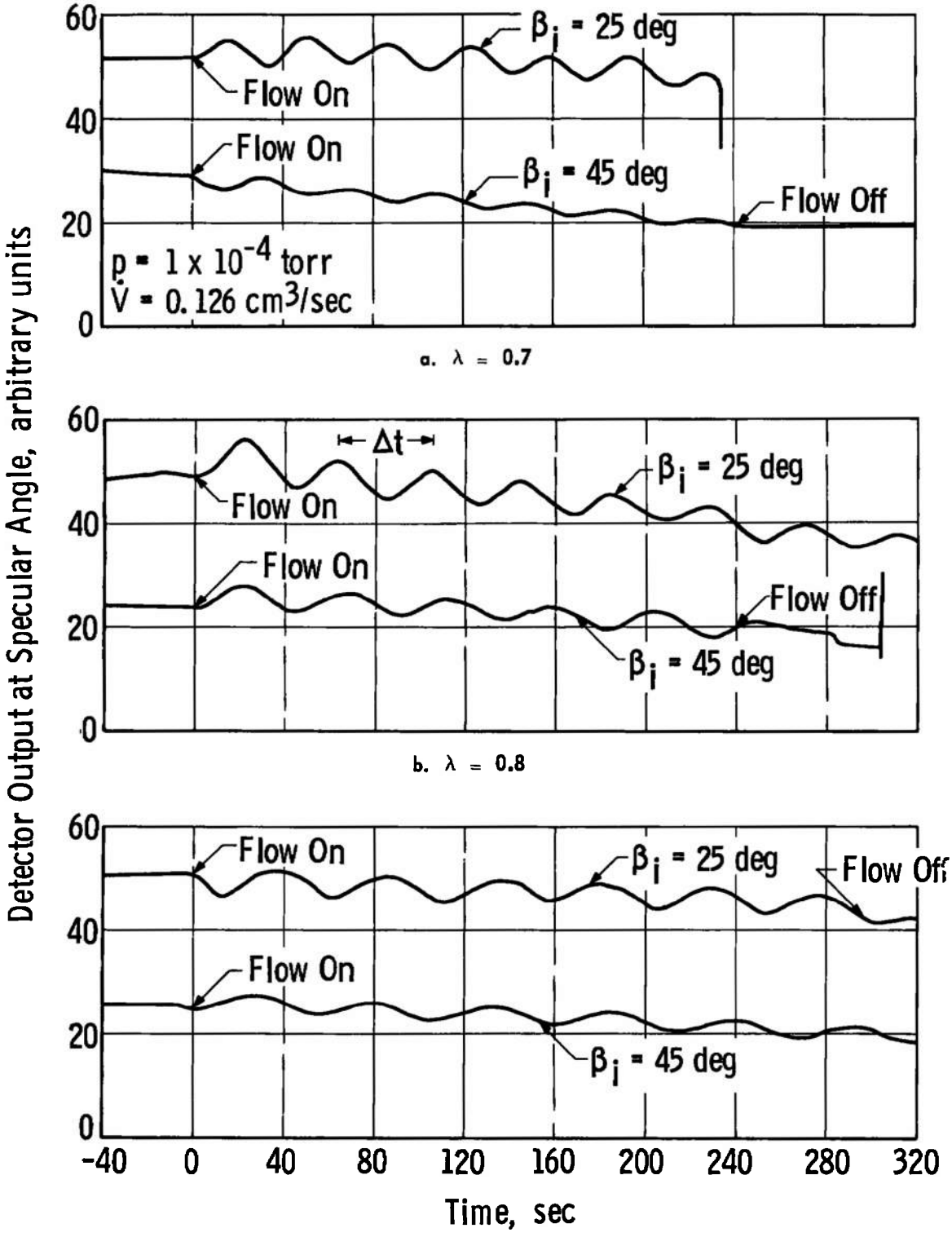


Fig. 14 Bragg Refraction Patterns for $CO_2$ Cryodeposits with Various Wavelengths of Incident Radiation

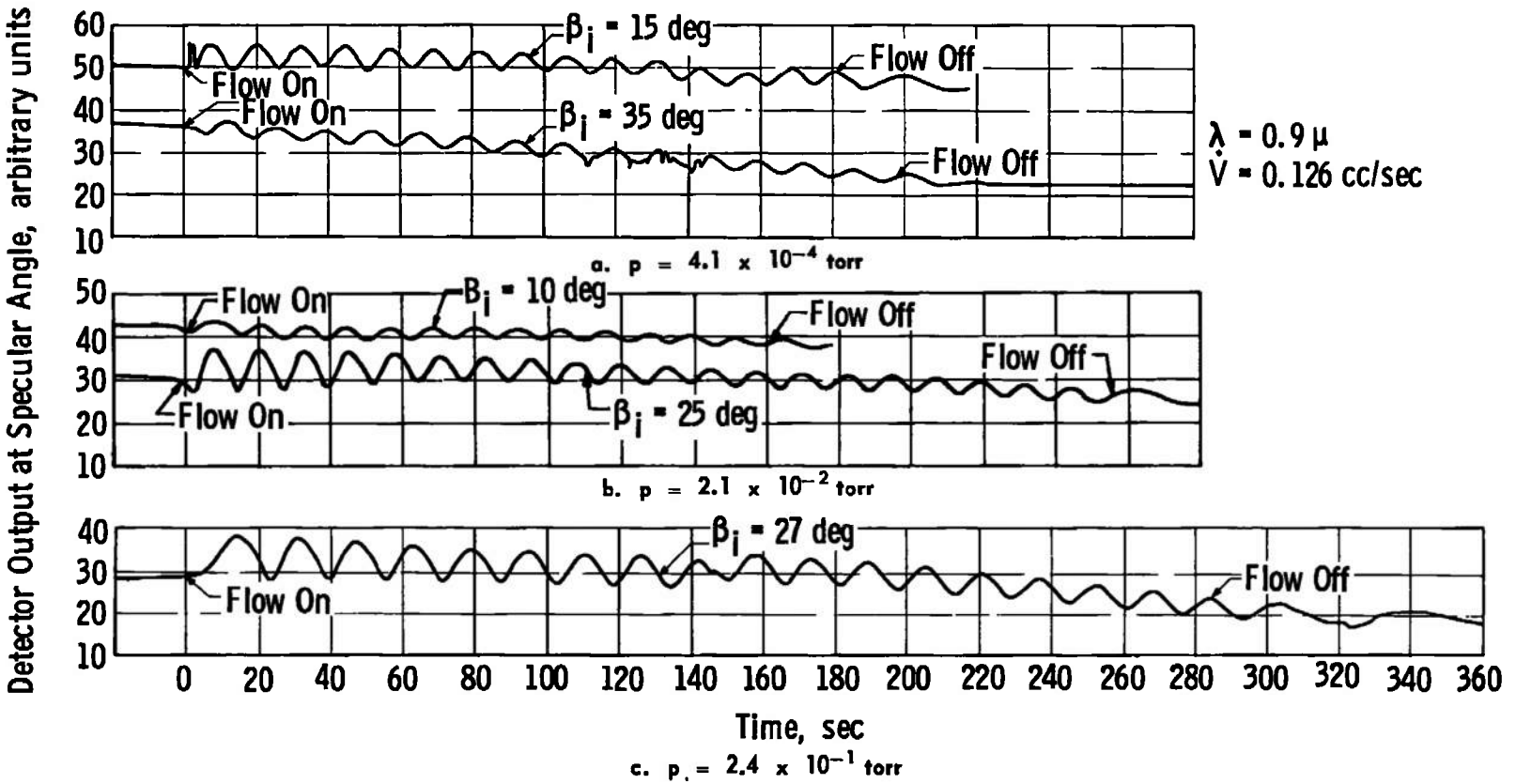


Fig. 15 Bragg Refraction Patterns for $CO_2$ Cryodeposits Formed at Various Pressure Levels

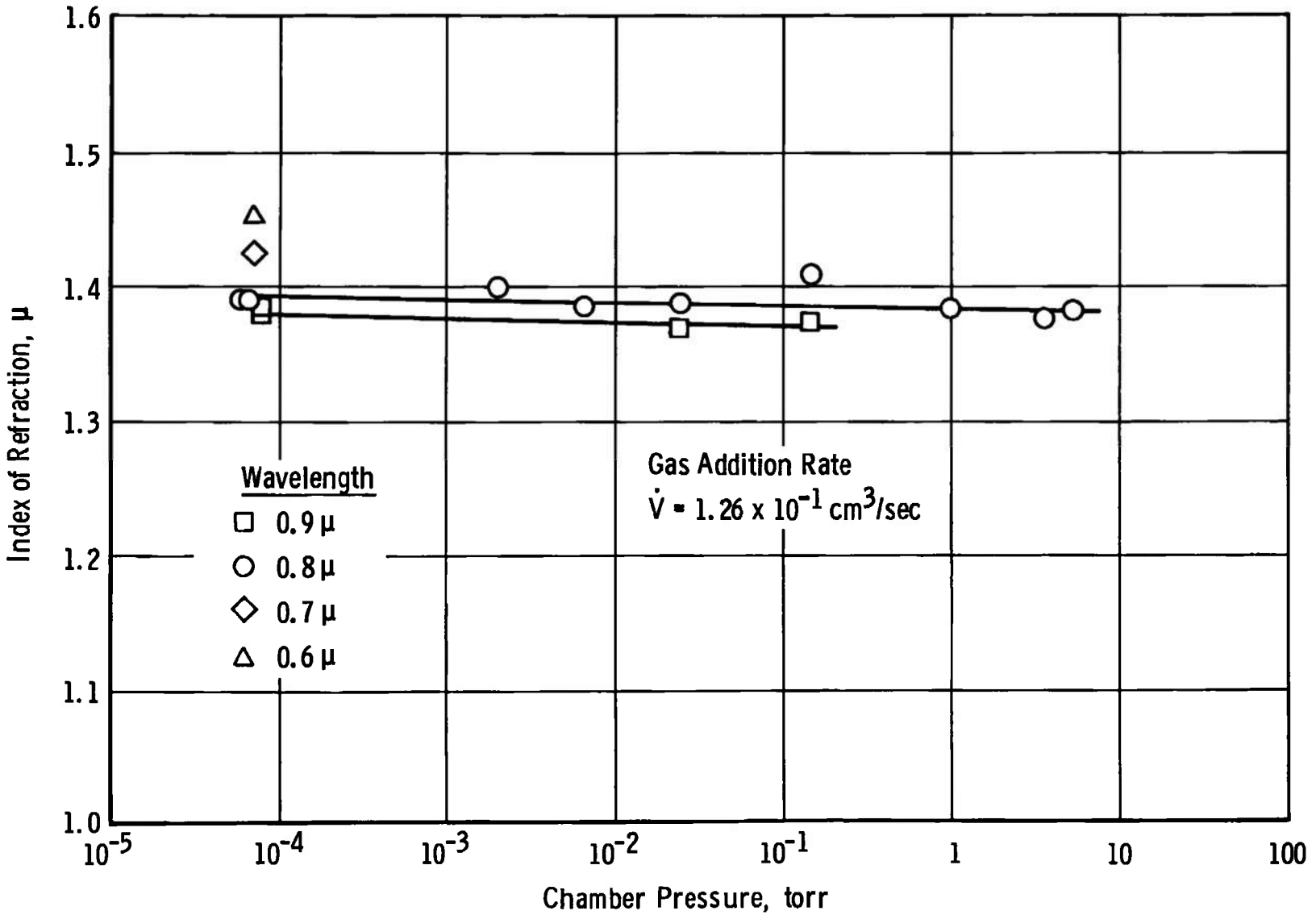


Fig. 16 Measured Refraction Index for $CO_2$ Cryodeposits at Various Pressure Levels and Wavelengths

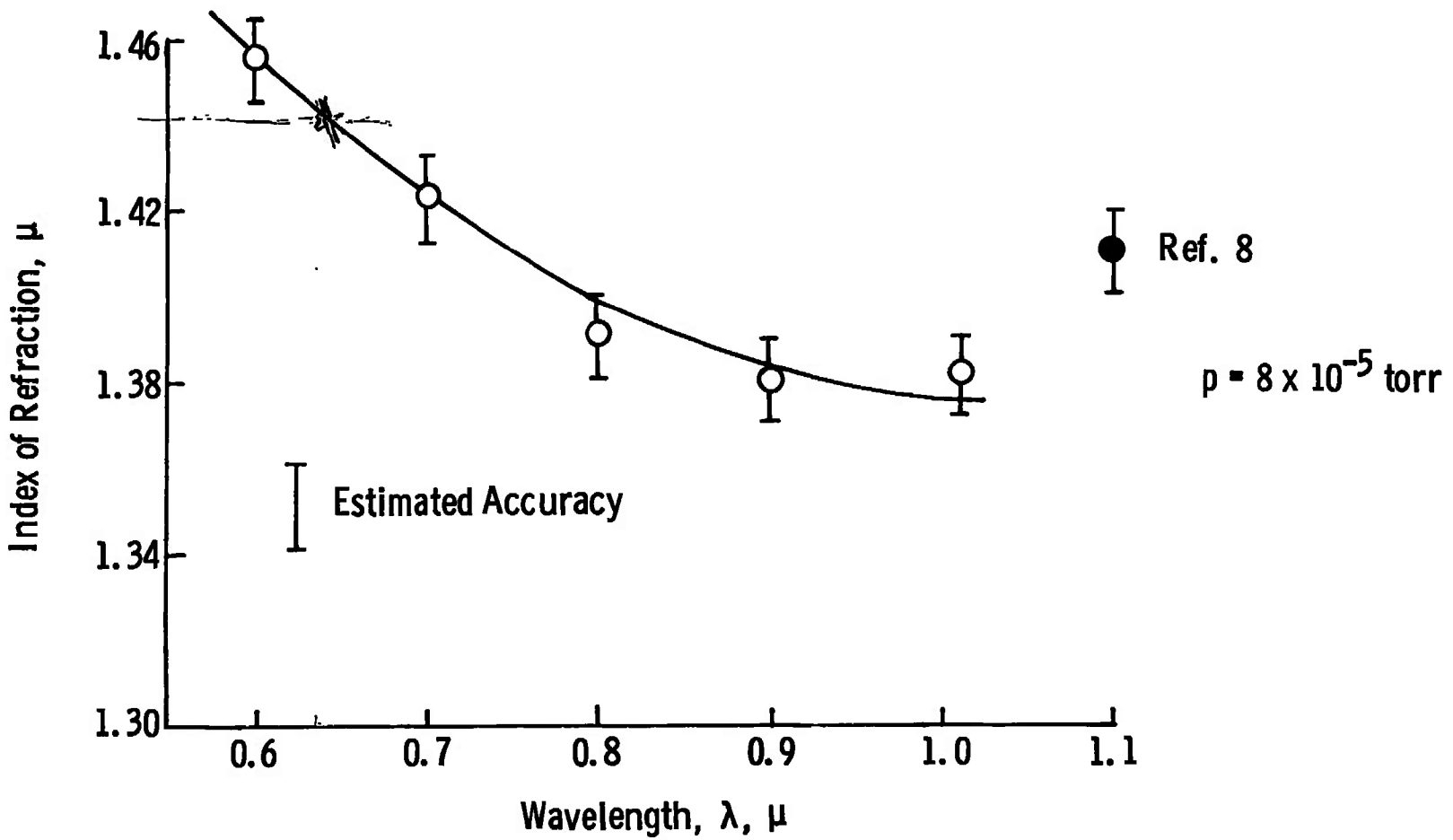


Fig. 17 Variation of Refractive Index of $CO_2$ Cryodeposit with Wavelength

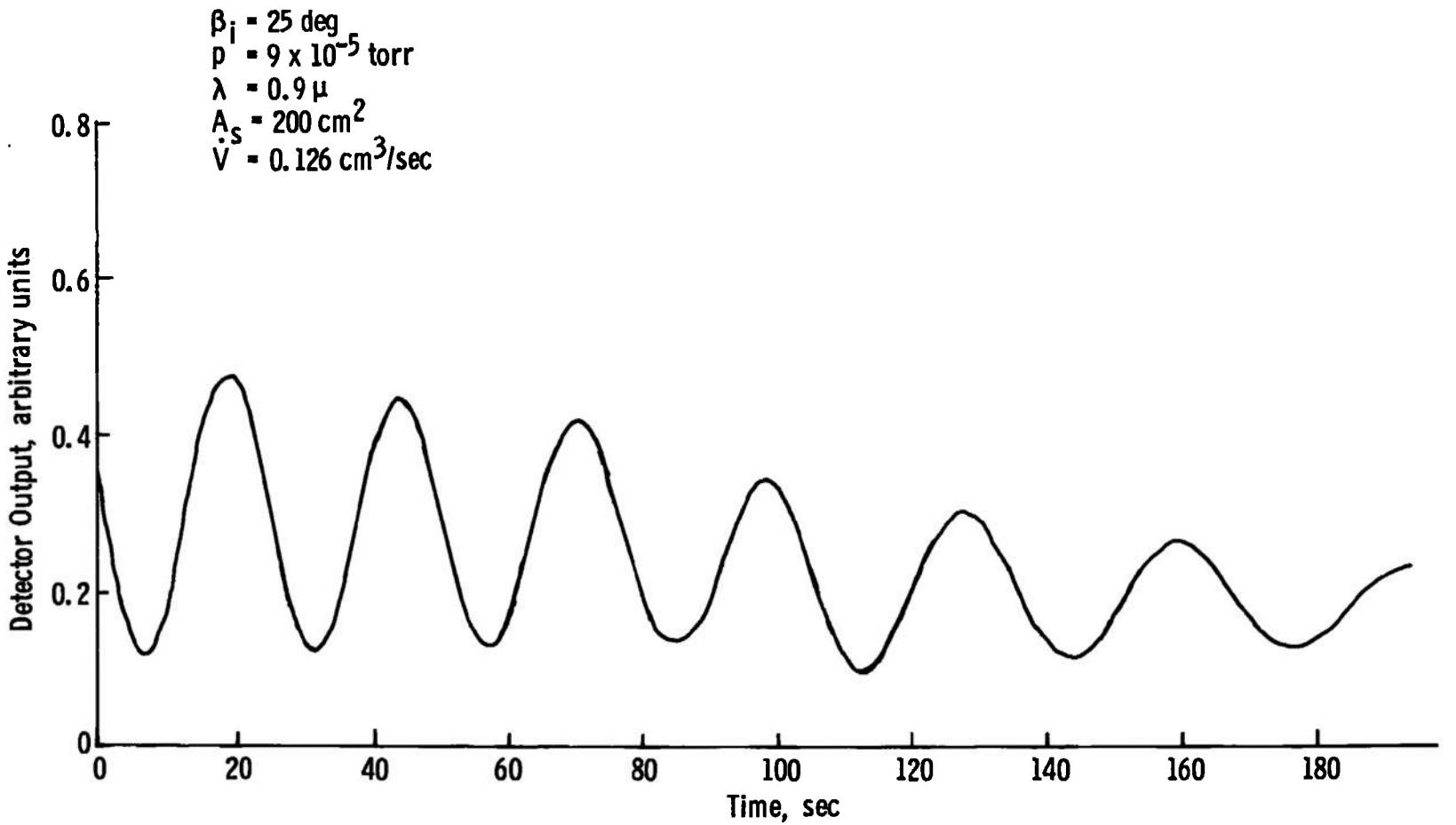


Fig. 18 Bragg Interference from 77°K $CO_2$ Cryodeposits on a Black Substrate

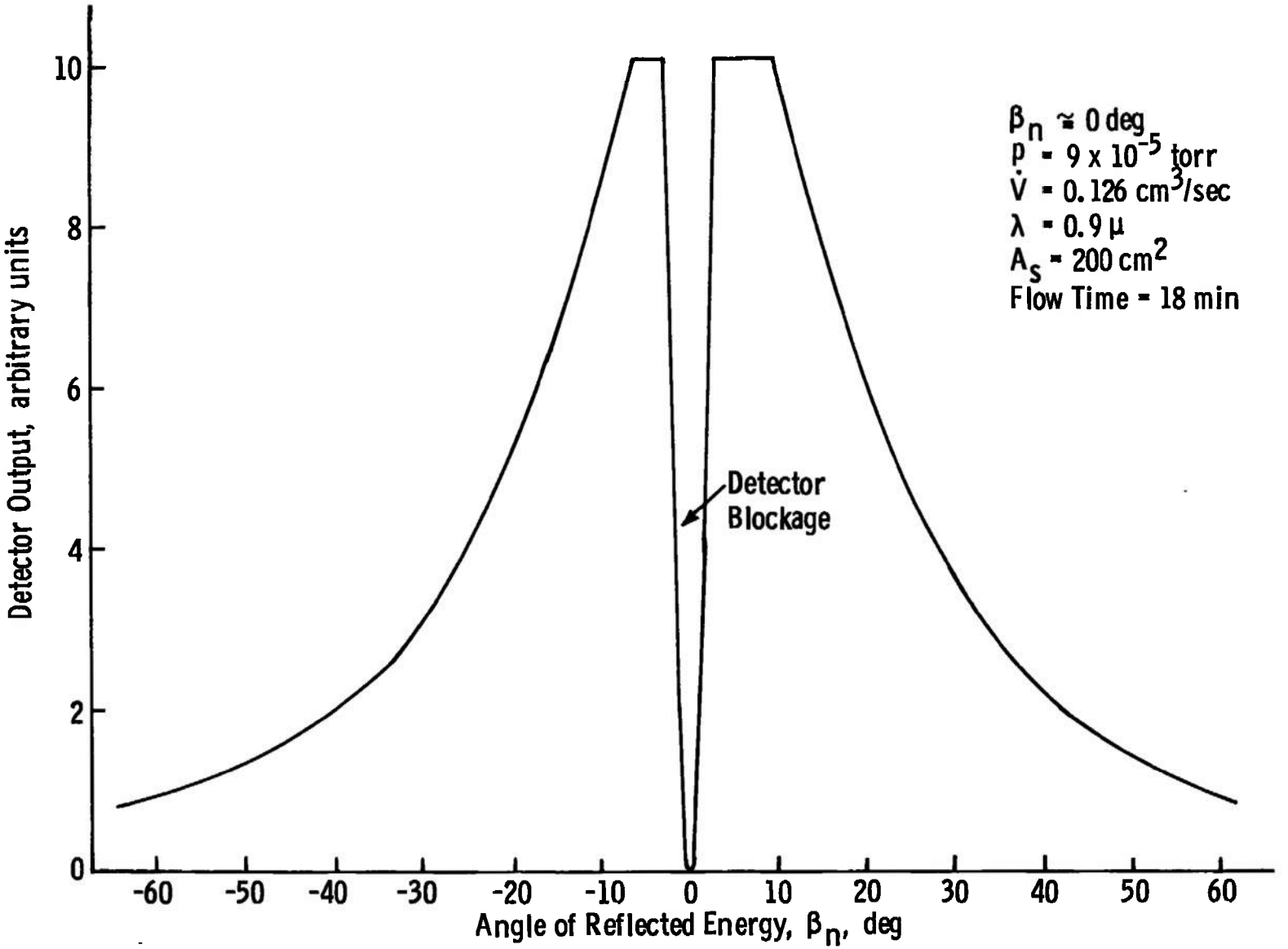


Fig. 19 Angular Distribution of Light from a 77°K $CO_2$ Cryodeposit on a Black Substrate

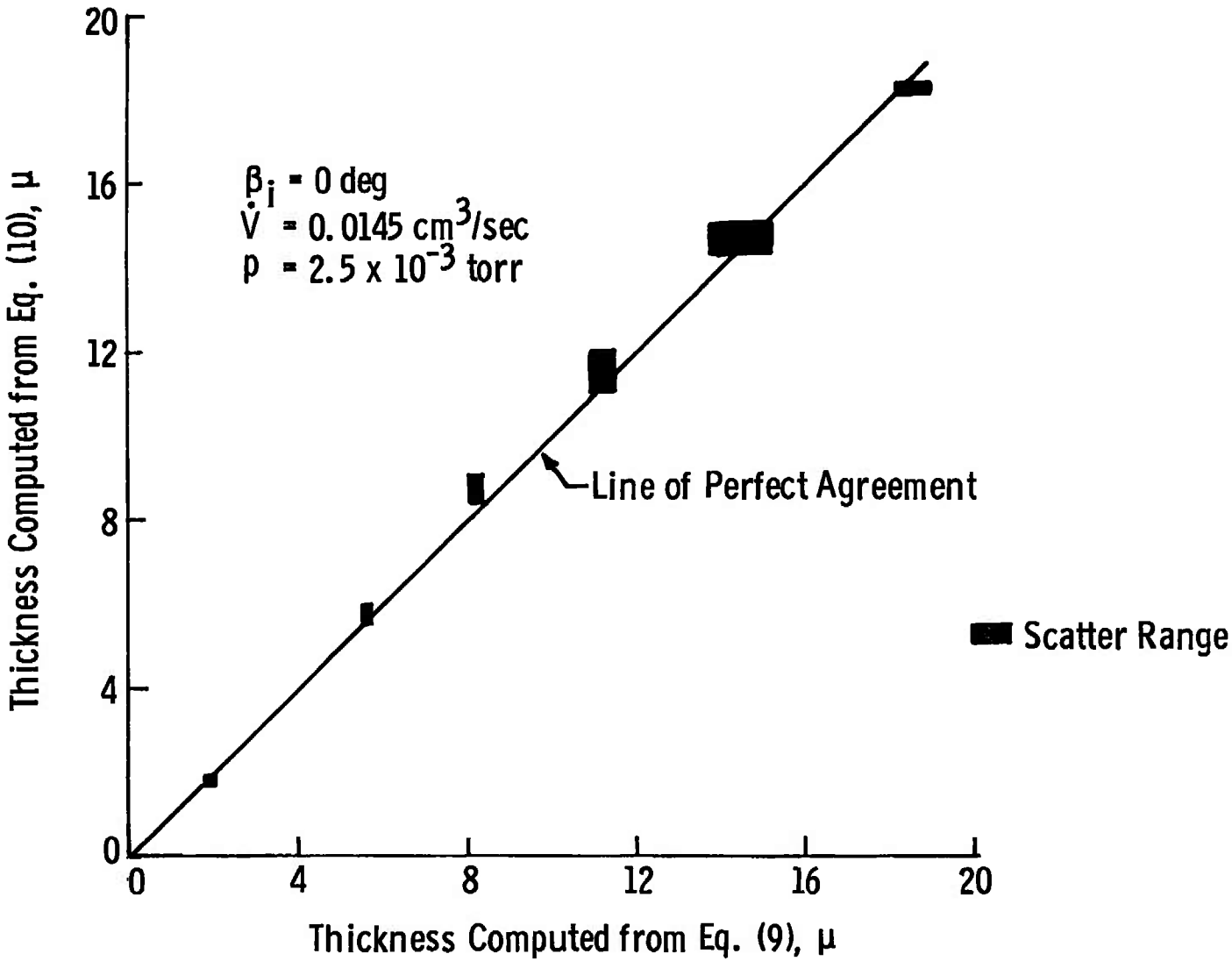


Fig. 20 Comparison of Calculated Thicknessess

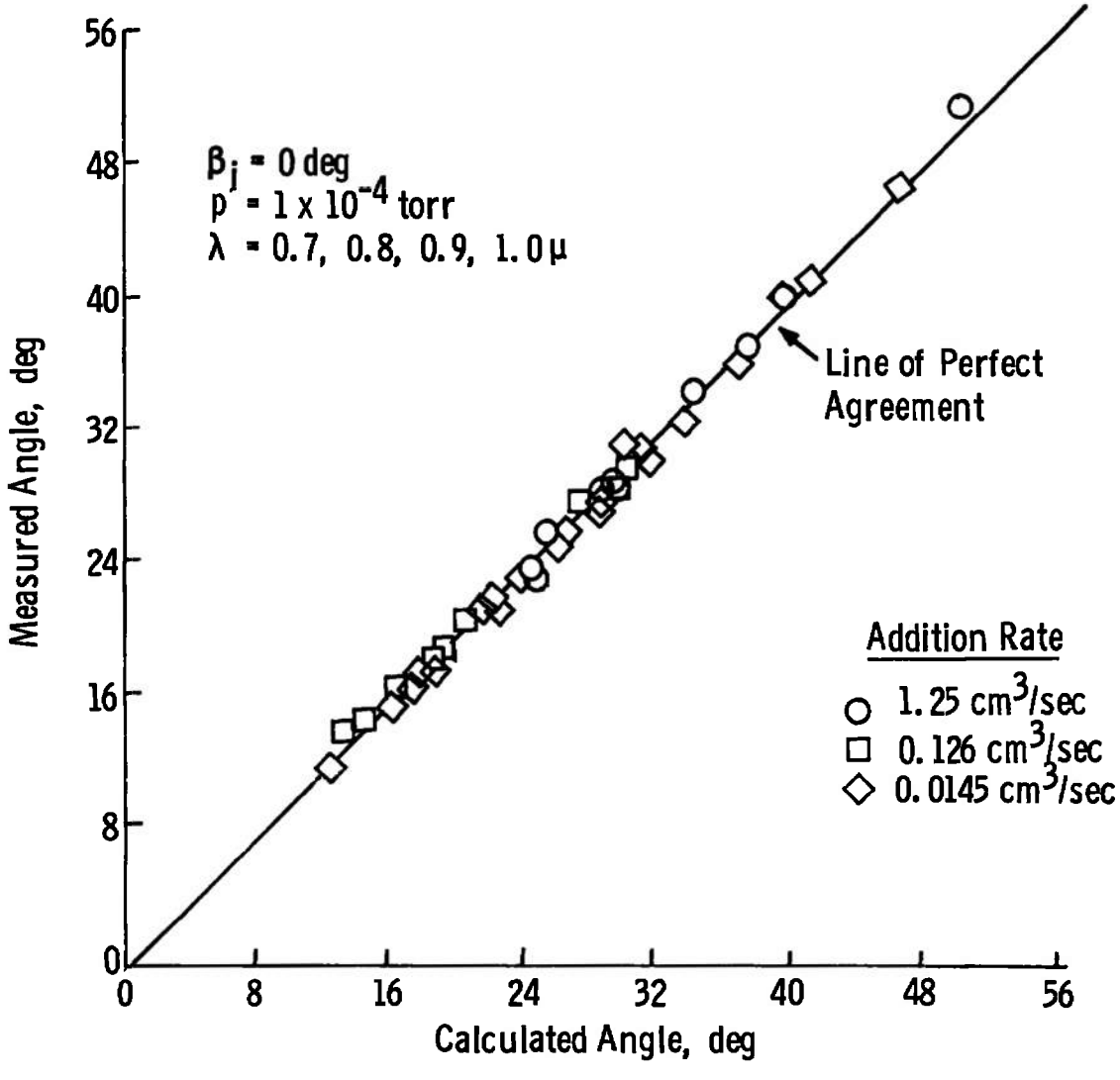


Fig. 21 Calculation of Nth Order Peak Locations

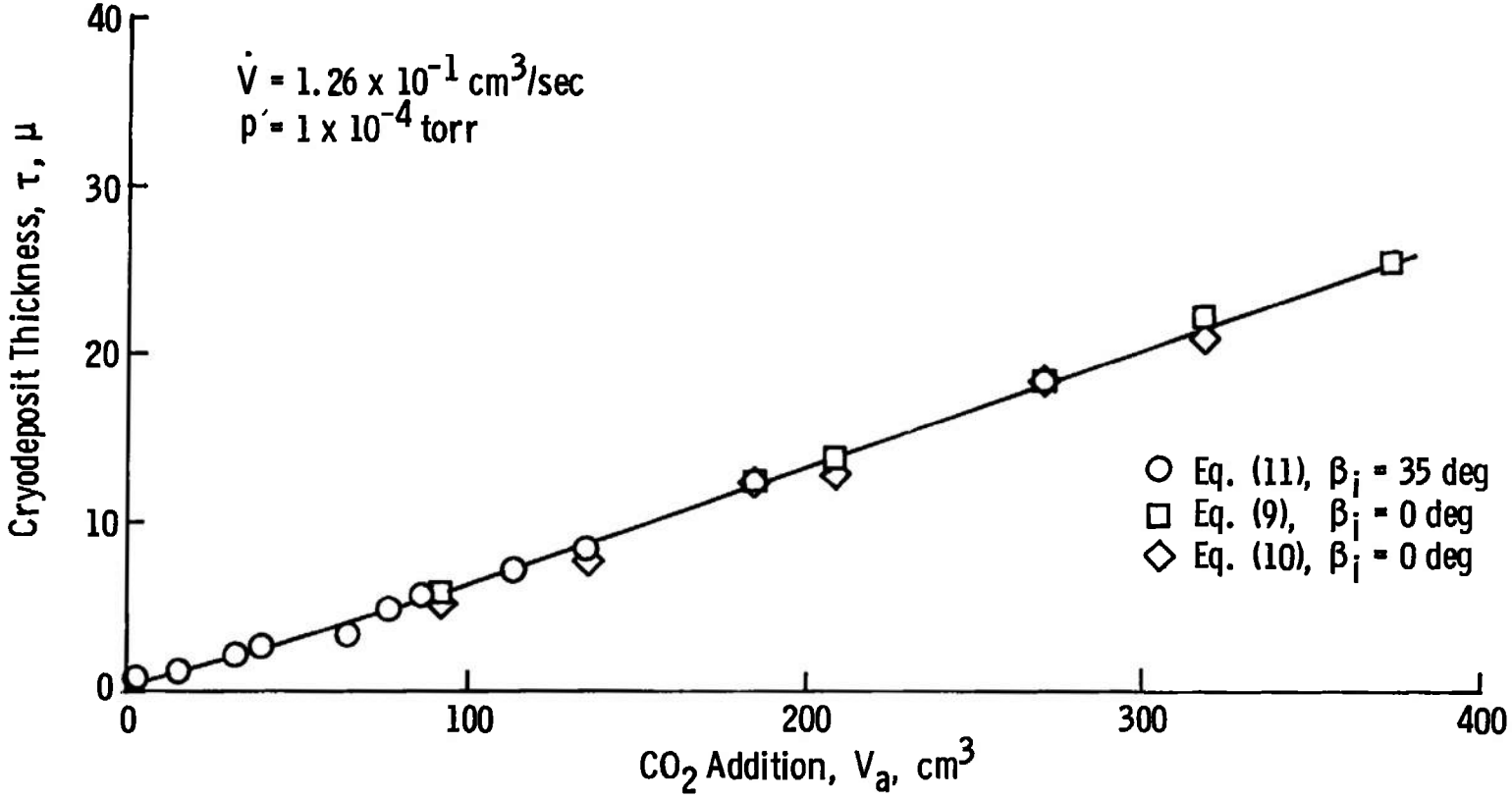


Fig. 22 Comparison of Various Methods of Computing Cryodeposit Thicknesses

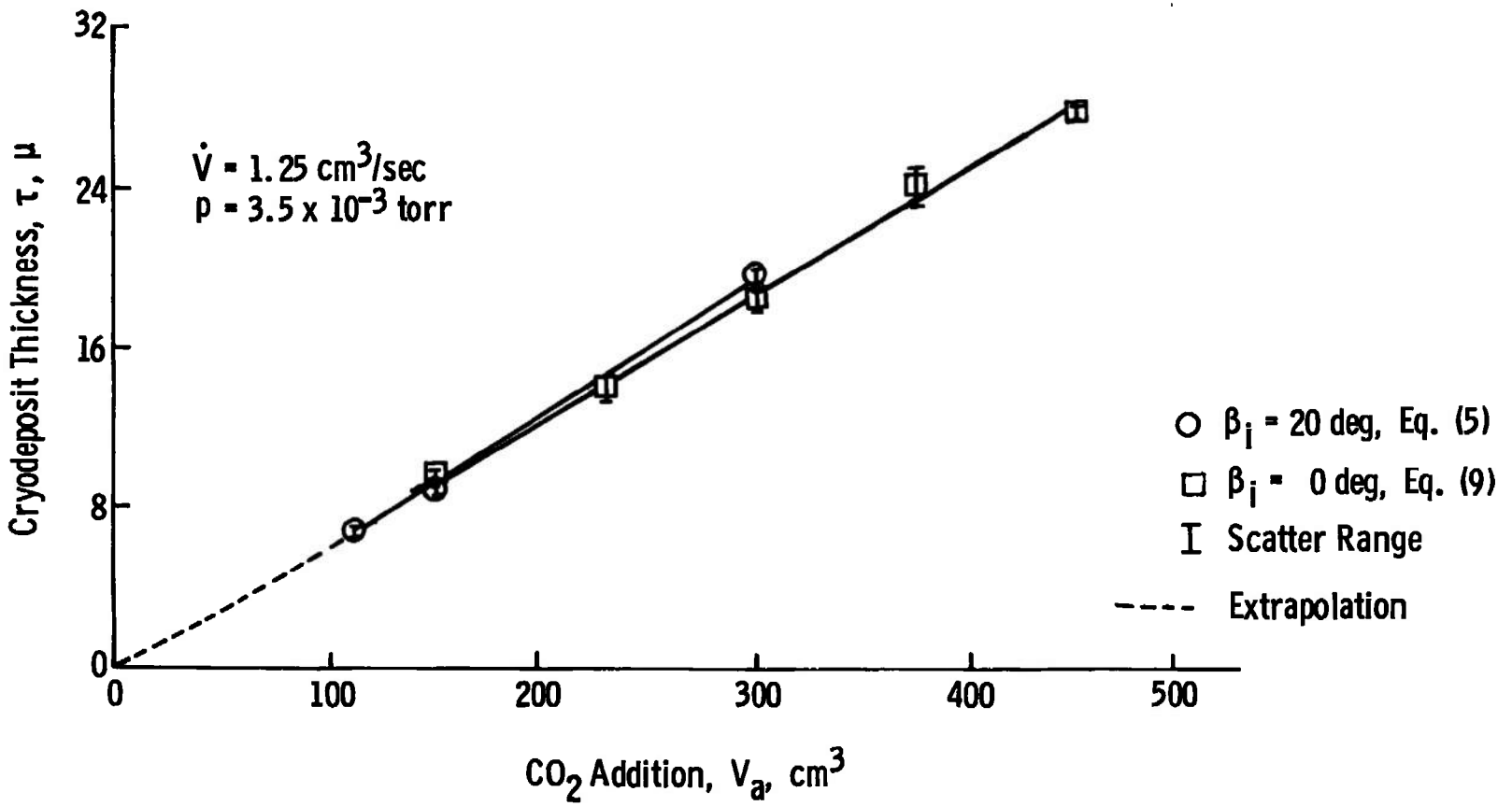


Fig. 23 Comparison of Cryodeposit Thickness Determined with Incident Radiation at Two Angles

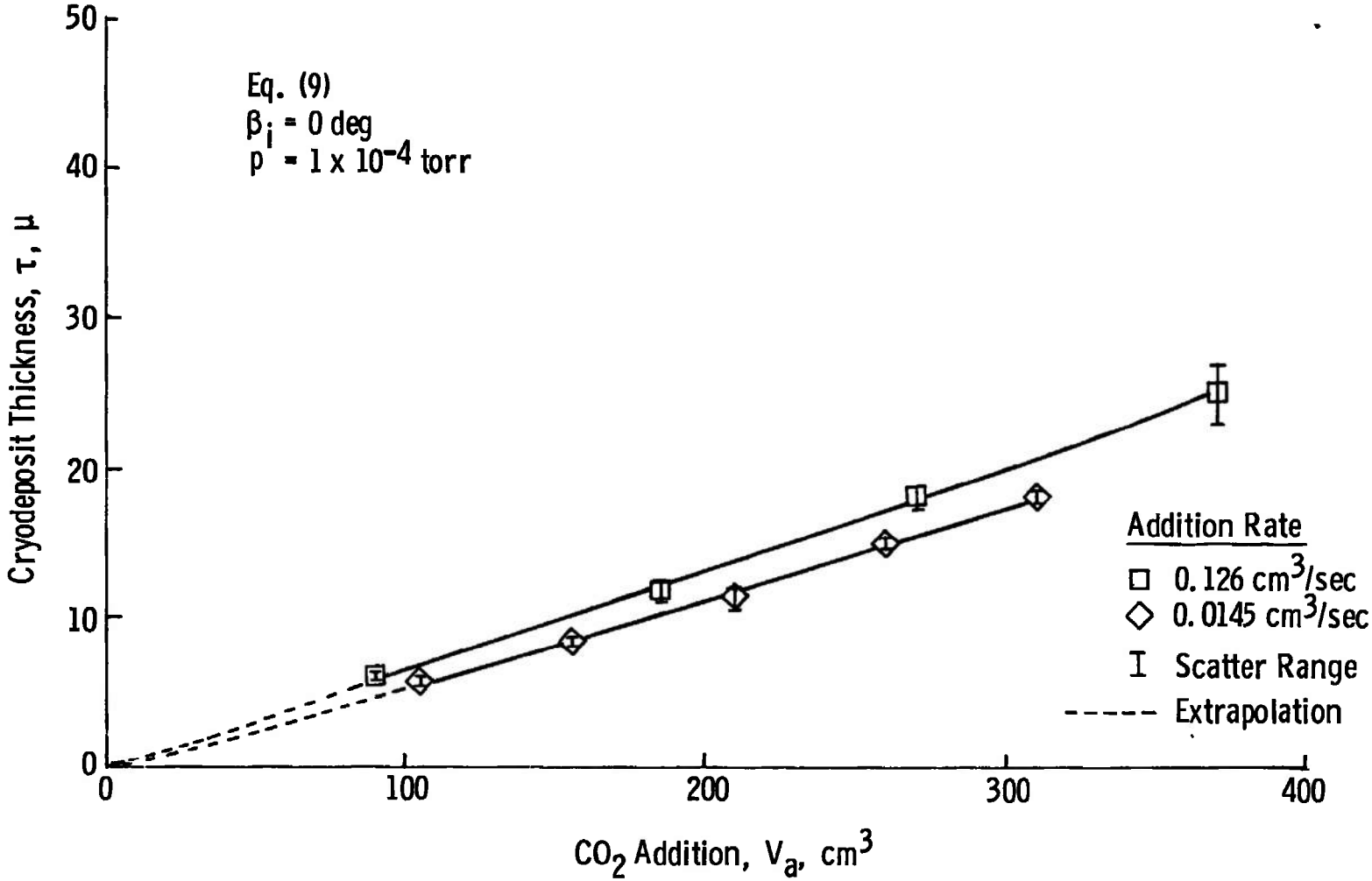


Fig. 24 Effect of Gas Addition Rate on Cryodeposit Thickness

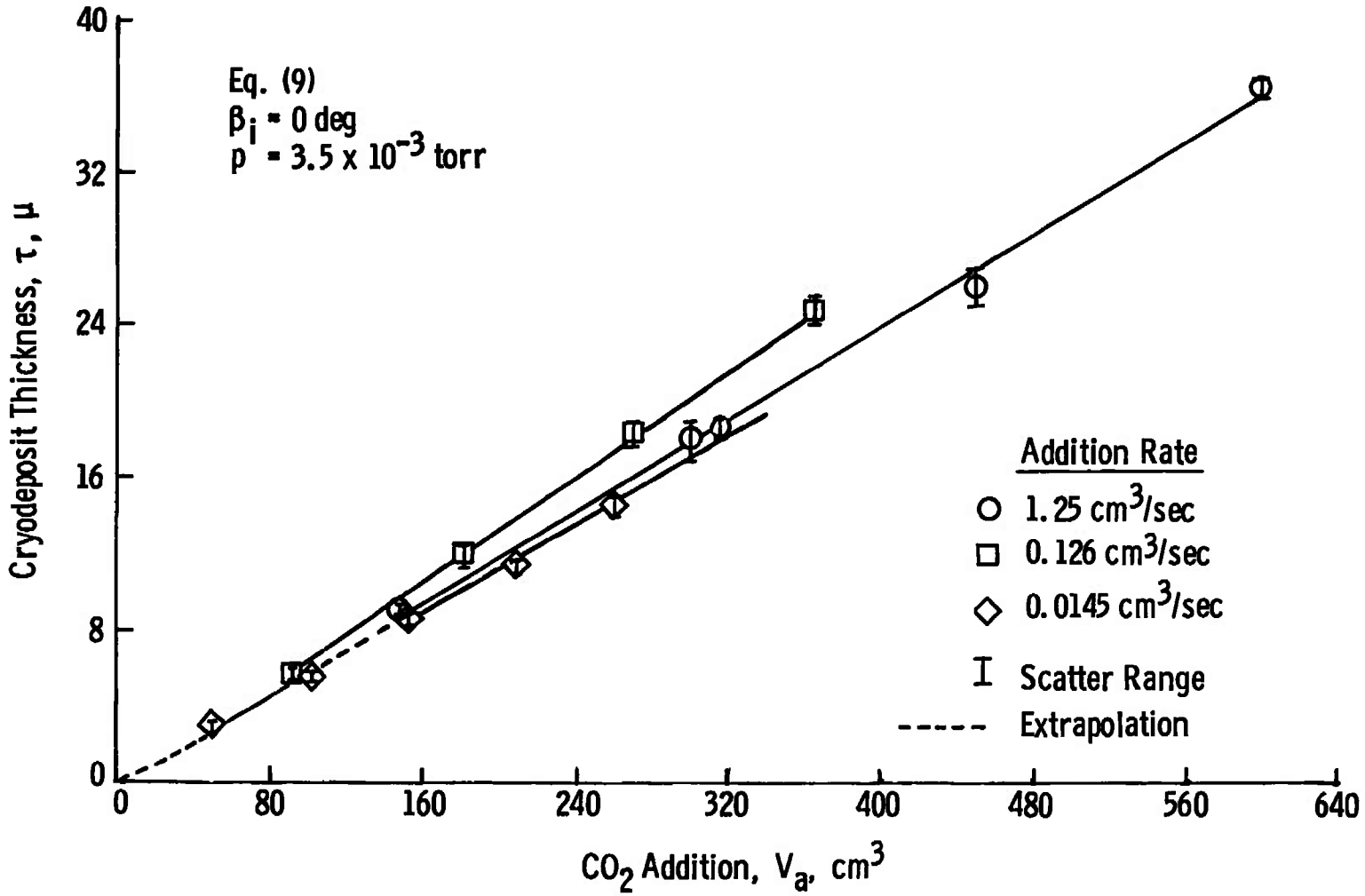


Fig. 25 Effect of Gas Addition Rate on Cryodeposit Thickness

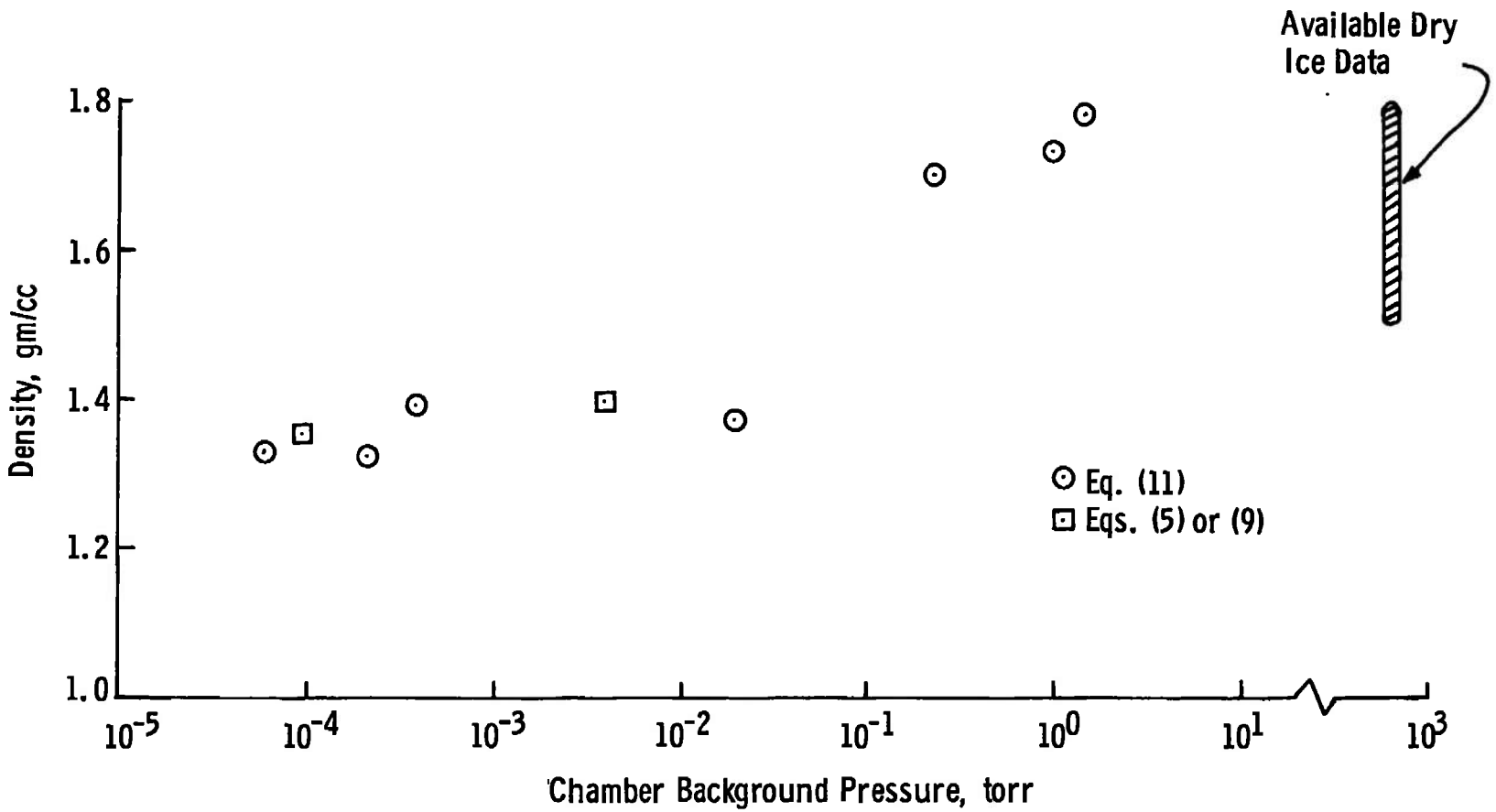


Fig. 26 Density of $CO_2$ Cryodeposits at Various Pressures

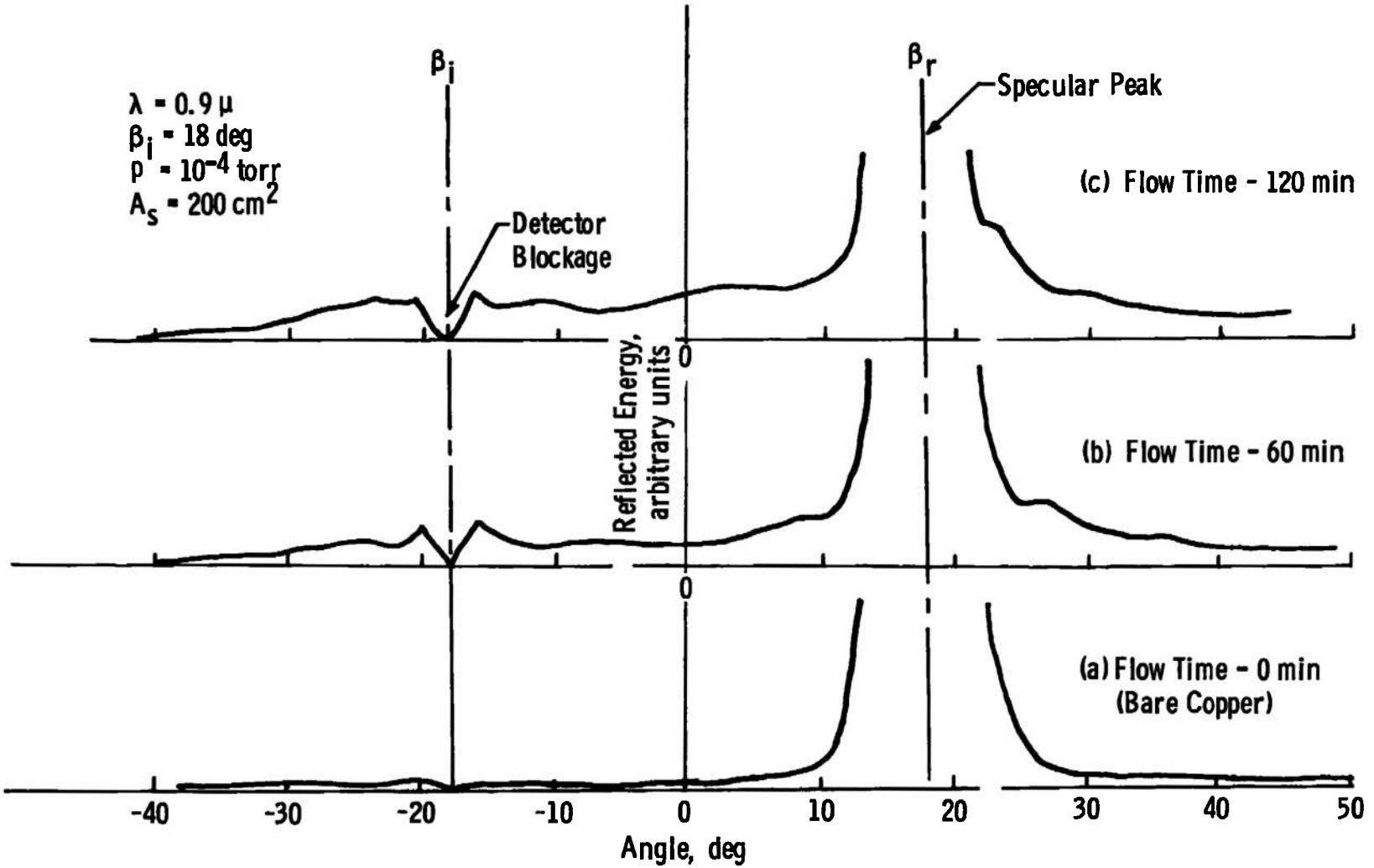


Fig. 27 Scattering Interference Patterns for 77°K $H_2O$ Cryodeposits at Two Thicknesses

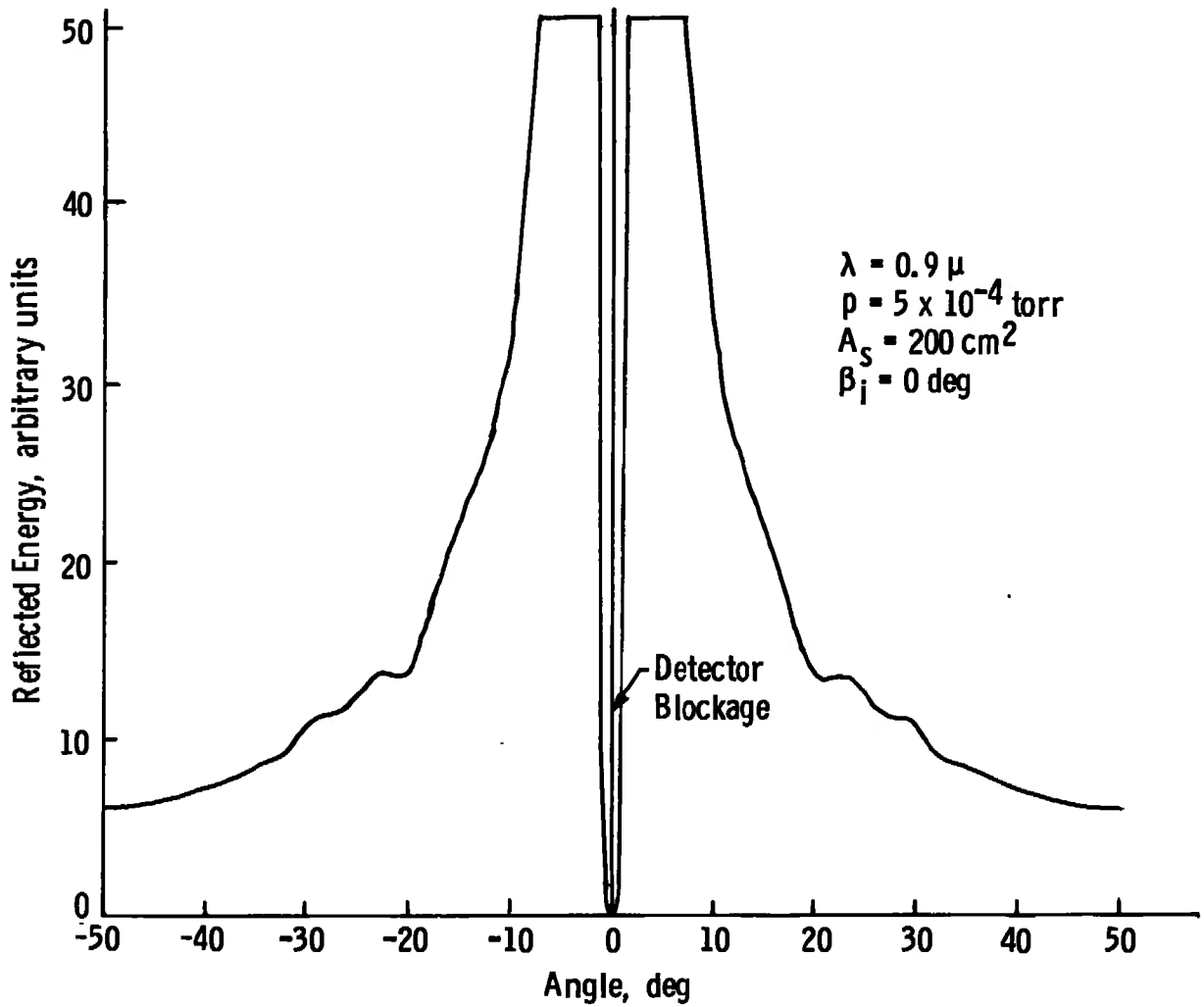


Fig. 28 Bragg and Scattering Interference Patterns for 77°K Cryodeposits of Diffusion Pump Oil

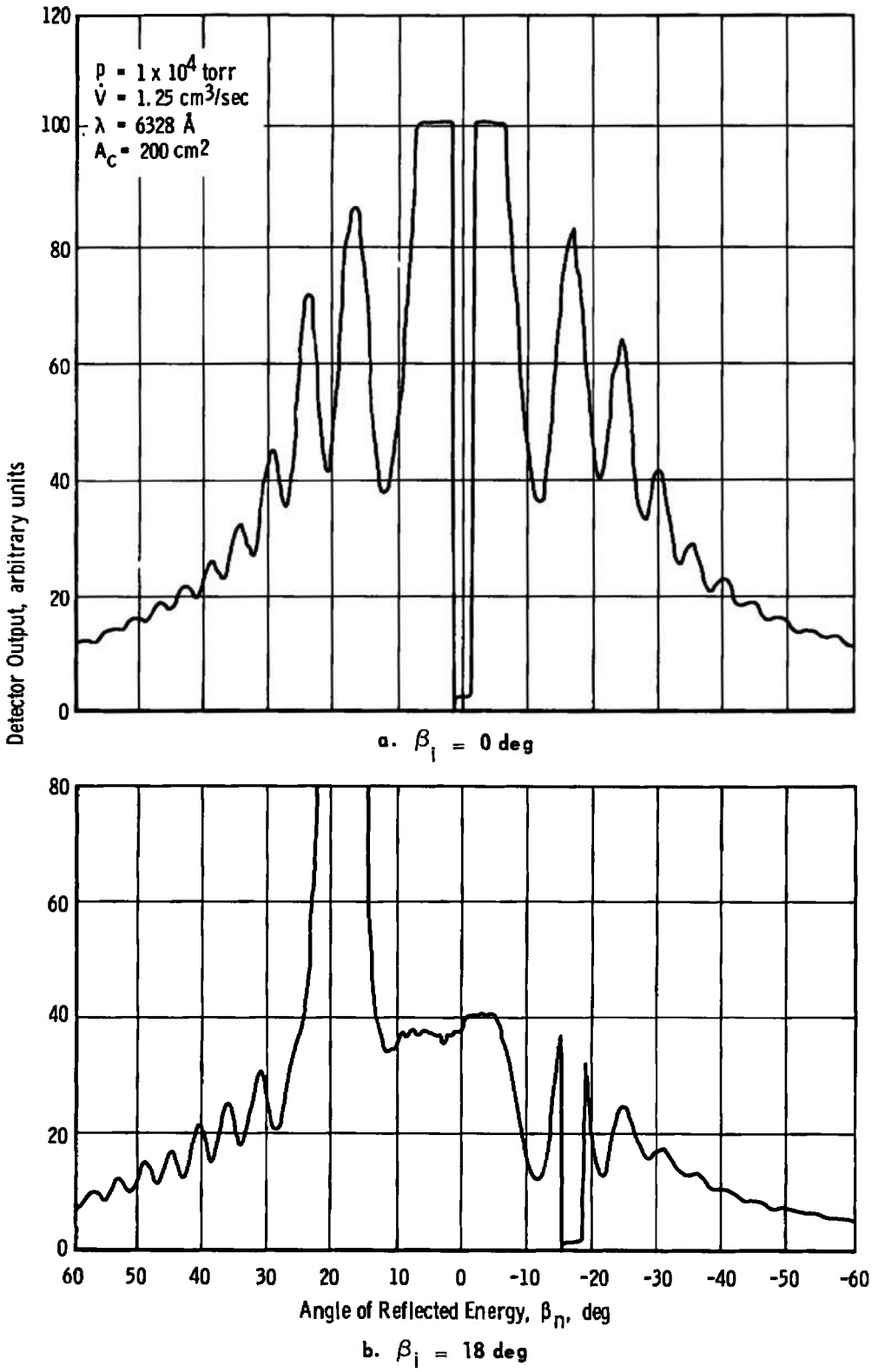


**Fig. 29 Scattering Interference Patterns of $CO_2$ Cryodeposit with a Laser Light Source**

# APPENDIX II
# METHODS OF CALCULATION

From Eq. (6), it is seen that $m_1$ must be known in order to use Eq. (5). The required values of m are

$$m = m_1 \text{ for } \beta_1$$
$$m = m_1 - 1 \text{ for } \beta_2$$
$$m = m_1 - 2 \text{ for } \beta_3$$
$$\cdot$$
$$\cdot$$
$$m = m_1 - a \text{ for } \beta_{(a+1)}$$

where a is the number of interference peaks observed for $\beta_n$ greater than $\beta_1$. For example, $m_1$ is the order of the first observed peak at $\beta_1$ and $(n_1 - a)$ is the order of the (a + 1) observed peak which occurs at $\beta_{(a+1)}$. By substituting these values into Eq. (5), the following ratio can be obtained:

$$\frac{m_1}{m_1 - a} = \frac{\dfrac{2\mu r}{\lambda}\sqrt{1 - \dfrac{\sin^2\beta_1}{\mu^2}}}{\dfrac{2\mu r}{\lambda}\sqrt{1 - \dfrac{\sin^2\beta_{(a+1)}}{\mu^2}}} = \frac{\sqrt{1 - \dfrac{\sin^2\beta_1}{\mu^2}}}{\sqrt{1 - \dfrac{\sin^2\beta_{(a+1)}}{\mu^2}}}$$

This can be simplified to

$$m_1 = \frac{a}{1 - \dfrac{\sqrt{1 - \dfrac{\sin^2\beta_{(a-1)}}{\mu^2}}}{\sqrt{1 - \dfrac{\sin^2\beta_1}{\mu^2}}}}$$

The closest integer to the value of $m_1$ obtained from the above equation is the order of the interference peak occurring at $\beta_i$. The remaining integers $(m_1 - 1)$, $(m_1 - 2)$ to $(m_1 - a)$ are then easily found.

Security Classification

## DOCUMENT CONTROL DATA - R & D

*(Security classification of title, body of abstract and indexing annotation must be entered when the overall report is classified)*

| | |
|---|---|
| 1. ORIGINATING ACTIVITY *(Corporate author)*<br>Arnold Engineering Development Center<br>ARO, Inc., Operating Contractor<br>Arnold Air Force Station, Tennessee | 2a. REPORT SECURITY CLASSIFICATION<br>UNCLASSIFIED<br>2b. GROUP<br>N/A |

3. REPORT TITLE

IN SITU MEASUREMENT OF THICKNESS AND OTHER PROPERTIES OF CARBON DIOXIDE CRYODEPOSITS BY OPTICAL TECHNIQUES

4. DESCRIPTIVE NOTES *(Type of report and inclusive dates)*

Jan. 1 to July 31, 1967

5. AUTHOR(S) *(First name, middle initial, last name)*

K. E. Tempelmeyer, B. E. Wood, and D. W. Mills, Jr., ARO, Inc.

| | | |
|---|---|---|
| 6. REPORT DATE<br>December 1967 | 7a. TOTAL NO. OF PAGES<br>61 | 7b. NO. OF REFS<br>8 |
| 8a. CONTRACT OR GRANT NO.<br>AF 40(600)-1200<br>b. PROJECT NO. 8951<br>c. Program Element 6144501F<br>d. Task 895104 | 9a. ORIGINATOR'S REPORT NUMBER(S)<br>AEDC-TR-67-226<br>9b. OTHER REPORT NO(S) *(Any other numbers that may be assigned this report)*<br>N/A | |

10. DISTRIBUTION STATEMENT

This document has been approved for public release and sale; its distribution is unlimited.

| | |
|---|---|
| 11. SUPPLEMENTARY NOTES<br>Available in DDC | 12. SPONSORING MILITARY ACTIVITY<br>Arnold Engineering Development Center<br>Air Force Systems Command<br>Arnold Air Force Station, Tennessee |

13. ABSTRACT

Measurements of interference patterns in filtered light reflected from thin 77°K $CO_2$ cryodeposits are reported. Analysis indicated that these patterns are a result of interference between light rays scattered by reflection from the cryodeposit surface with rays which are scattered by passage through the surface and specularly reflected by the substrate. A simple light scattering model for cryodeposits is proposed which allows accurate determination of the deposit thickness from the interference patterns. Application of the scattering theory required knowledge of the refractive index of the cryodeposit. Consequently, the index of refraction for $CO_2$ cryodeposits was determined from separate Bragg interference tests at wavelengths from 0.6 to 1.0 $\mu$. Cryodeposit thicknesses up to 100 $\mu$ have been determined from the scattering model equation. Utilizing mass conservation principles, the thickness calculations were further used to determine the mean cryodeposit density. A few scattering interference tests on other types of cryodeposits are also briefly reported.

DD FORM 1 NOV 65 1473

Security Classification

| 14 KEY WORDS | LINK A ROLE | LINK A WT | LINK B ROLE | LINK B WT | LINK C ROLE | LINK C WT |
|---|---|---|---|---|---|---|
| cryodeposits | | | | | | |
| carbon dioxide | | | | | | |
| cryopumping | | | | | | |
| measurement techniques | | | | | | |
| thickness measurements, optical | | | | | | |